Appendices

- **Electronic Supplement A: Further description of the case study**
- **Electronic Supplement B: Further description of methodological aspects**
- **Electronic Supplement C: Additional results**

A Electronic Supplement A: Further description of the case study

A.1 Sites and events considered

The locations of the four SMS sites and two earthquakes considered in this study are illustrated in Figure A.1.

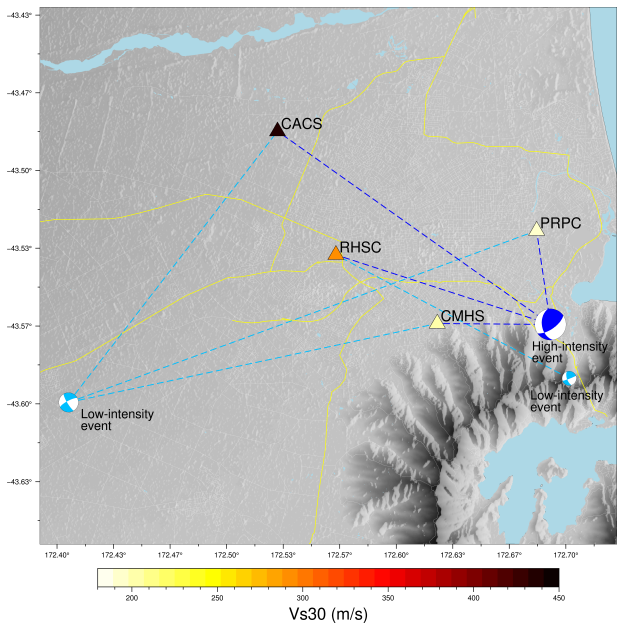

Figure A.1. Location of the strong-motion stations and events considered, and V_{S30} value of each site.

Table A.1 describes the three events and Table A.2 indicates the geometric mean horizontal PGA observed at each station during each earthquake.

Table A.1. Earthquakes considered.

Event Type	Event ID	Date	Magnitude (Mw)	Depth (km)
Low Intensity	3509905	09 May 2011	4.9	6.0
Low Intensity	2016p355041	11 May 2016	4.2	7.0
High Intensity	3468575	22 February 2011	6.2	4.0

Table A.2. Geometric mean horizontal PGA observed at the four strong-motion stations during the events considered.

Site	Low-Intensity Event		High-Intensity Event	
	Event ID	Observed PGA (g)	Event ID	Observed PGA (g)
PRPC	3509905	0.048	3468575	0.62
CMHS	3509905	0.048	3468575	0.37
RHSC	2016p355041	0.020	3468575	0.28
CACS	3509905	0.031	3468575	0.19

A.2 Site-characterization data

A.2.1 Site PRPC - Pages Road Pumping Station The site-characterization data used in this study to characterize the site PRPC was obtained from Wotherspoon et al. (2015). Figure A.2 shows the location of the site-characterization data available (including V_S, HVSR, CPT, SPT, and borehole data) relative to the strong-motion station (represented by a yellow circle).

Figure A.2. Location of the site-characterization data at the site PRPC (Wotherspoon et al. 2015).

Figure A.3 shows the site-specific V_s profile and CPT data used to characterize the site PRPC. The V_S profile used corresponds to the linear array SW1 and the CPT utilized is CPT1, which is the closest to the station and the deepest one available. CPT1 reached refusal at a depth of 28 m, which is consistent with the increase of V_S at that depth and suggests the start of the Riccarton Gravel Formation. Figure A.3 also presents the V_S

profiles derived by two different CPT-V_S correlations (Robertson 2009; McGann et al. 2015), showing that the Christchurch-specific correlation developed by McGann et al. (2015) is fairly consistent with the geophysical estimate. The water table measured at borehole BH1 was 2.1 m and the value estimated from the CPT tests varied from 1.8 to 6.0 m. Regional maps (Van Ballegooy et al., 2014; Westerhoff et al., 2018) suggest a long-term average value between 0.0 and 2.5 m. A value of 2.2 m was chosen as representative for this site.

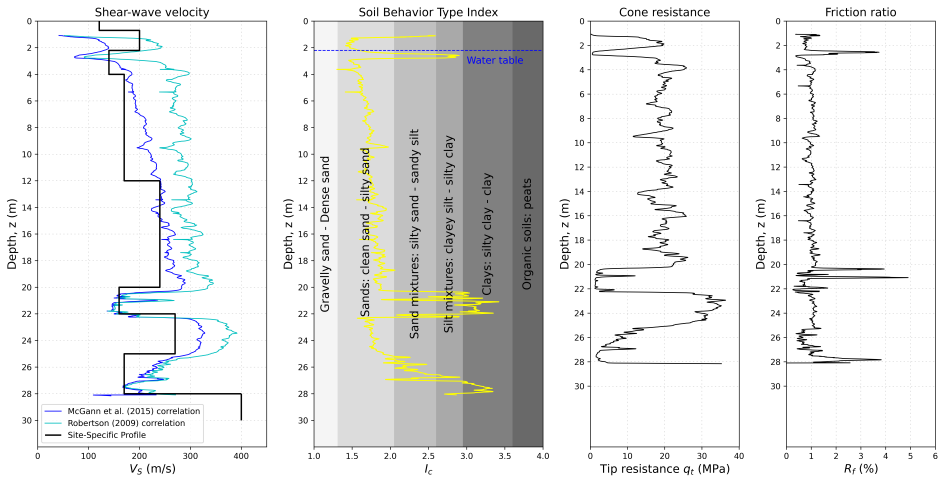

Figure A.3. V_S and CPT data used to characterize the site PRPC.

Table A.3 provides an interpreted stratigraphy of the site PRPC down to 30 m depth, based on the site-characterization data available.

Table A.3. PRPC stratigraphy down to 30 m depth.

Depth (m)	Description	Vs (m/s)
0.0 - 20.0	Sand and silty sand	121 to 240
20.0 - 22.0	Silty clay	160
22.0 - 25.0	Sand and silty sand	270
25.0 - 28.0	Silty sand to silty clay	170
28.0 - 30.0	Riccarton Gravels	400

A.2.2 Site CMHS - Cashmere High School Two sites investigations are available for the site CMHS and their locations are presented in Figure A.4 and Figure A.5. A site investigation performed within the close vicinity of the strong-motion station is provided

by Wotherspoon et al. (2015) (including V_S, HVSR, CPT, SPT, and borehole data), and a wider geophysical exploration performed with the purpose of deriving a deep shear-wave velocity profile is provided by Teague et al. (2018). According to Wotherspoon et al. (2015), this site is characterized by significant lateral variability.

Figure A.4. Location of the site-characterization data at the site CMHS provided by Wotherspoon et al. (2015).

Figure A.5. Location of geophyisical investigation at the site CMHS provided by Teague et al. (2018).

Figure A.6 shows the V_S profile SW1 obtained by Wotherspoon et al. (2015) and the median V_S profile obtained by Teague et al. (2018). As observed, these two profiles present differences in the first 30 m. As shown in Figure A.4, the profile SW1 was obtained from an array located fairly close to the strong-motion station (represented by a yellow circle). This V_S profile shows a V_S contrast at the depth of 13.8 m, which is coincident with the depth at which the Riccaron Gravels were found in the borehole BH1. Given that this profile seems to better represent the surficial stratigraphy of the site in the close proximity of the strong-motion station, and the median profile obtained by Teague et al. (2018) better contrains the deep velocity structure, a best-estimate V_S profile is derived here as the combination of both. Figure A.6 presents this V_S profile, which is used in this study as the representative profile for this site.

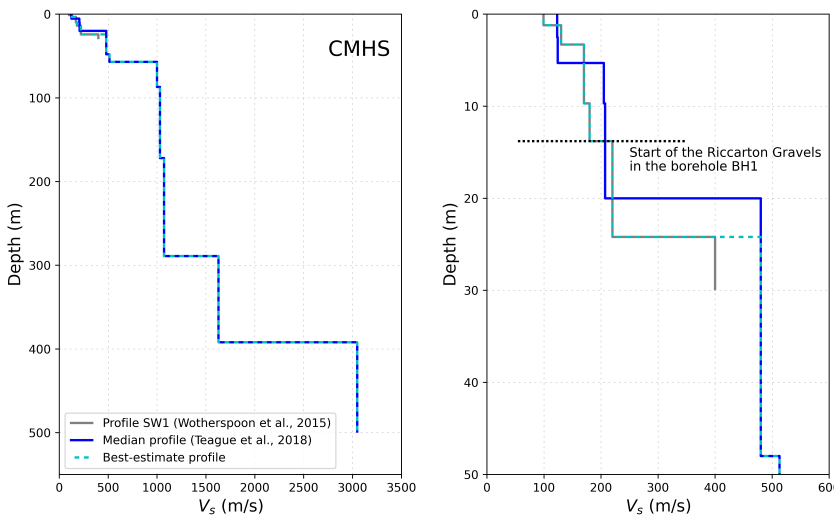

Figure A.6. Site characterization data at the strong-motion station CMHS.

Figure A.7 shows the site-specific V_S profile and CPT data used to characterize the site CMHS in this study. The CPT corresponding to CPT1, which is relatively close to the station and is the deepest one available. The water table measured at borehole BH1 was 2.0 m and the value estimated from the CPT tests varied from 1.8 to 3.6 m. Regional maps (Van Ballegooy et al., 2014; Westerhoff et al., 2018) suggest a long-term average value between 0.5 and 5.0 m. A value of 2.0 m was chosen as representative for this site.

Table A.4 provides an interpreted stratigraphy of the site CMHS down to 30 m depth, based on the available site-characterization data.

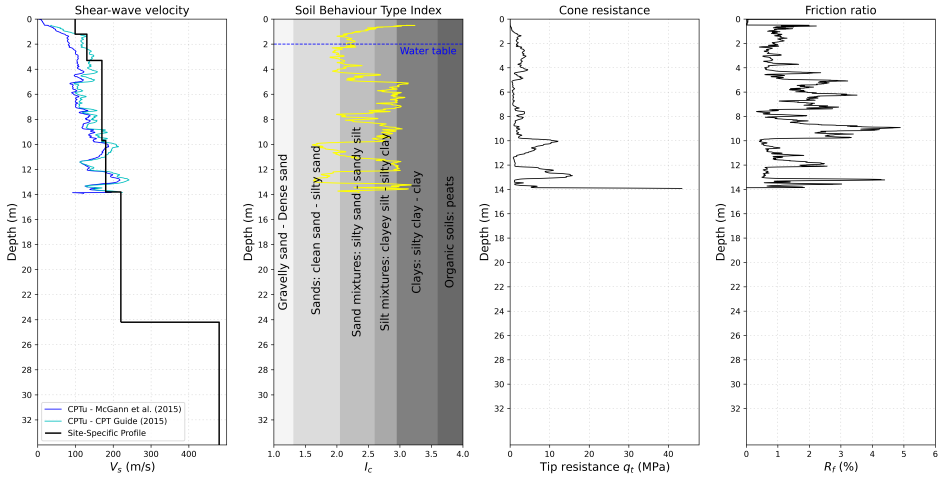

Figure A.7. V_S and CPT data used to characterize the site CMHS.

Table A.4. CMHS stratigraphy down to 30 m depth.

Depth (m)	Description	Vs (m/s)
0.0 - 13.8	Interbedded layers of sands and silts	99 - 180
13.8 - 30.0	Riccarton Gravels	220 - 480

A.2.3 Site RHSC - Riccarton High School Similar to the case of CMHS, two sites investigations are available for the site RHSC, and their locations are presented in Figure A.8 (including V_S, HVSR, SPT, and borehole data) and Figure A.9. A site investigation performed within the close vicinity of the strong-motion station is provided by Wotherspoon et al. (2015), and a more global geophysical exploration performed with the purpose of deriving a deep shear-wave velocity profile is provided by Teague et al. (2018).

Figure A.10 shows the V_S profile SW1 obtained by Wotherspoon et al. (2015) and the median V_S profile obtained by Teague et al. (2018). As observed, these two profiles present differences in the first 30 m. As shown in Figure A.8, the profile SW1 was obtained from an array located fairly close to the station. This V_S profile shows a V_S contrast at the depth of 6.5 m, which is coincident with the depth at which the Riccaron Gravels were found in the borehole BH1. Also, borehole BH1 shows very low values of SPT in the first 6.5 m, which is consistent with the low values of V_S observed in the V_S profile SW1. Given that this profile seems to better represent the surficial stratigraphy of the site in the close proximity of the strong-motion station, and the median profile

Figure A.8. Location of site investigations at the site RHSC provided by Wotherspoon et al. (2015).

Figure A.9. Location of site investigations at the site RHSC provided by Teague et al. (2018).

obtained by Teague et al. (2018) better contrains the deep velocity structure, a best-estimate V_S profile is derived here as the combination of both. Figure A.10 presents this V_S profile, which is used in this study as the representative profile for this site.

The water table measured at borehole BH1 was 6.4 m and regional maps (Van Ballegooy et al., 2014; Westerhoff et al., 2018) suggest a long-term average value between 0.0 and 7.0 m. A value of 6.45 m was chosen as representative for this site.

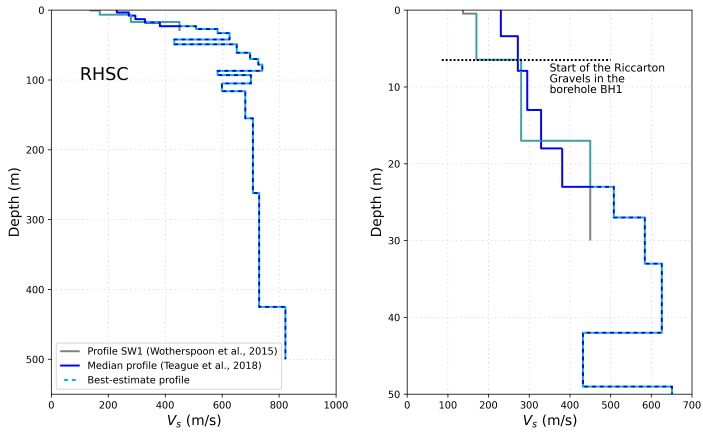

Figure A.10. Site characterization data at the strong-motion station RHSC.

Table A.5 provides an interpreted stratigraphy of the site RHSC down to 30 m depth, based on the all the available site-characterization data.

Table A.5. RHSC stratigraphy down to 30 m depth.

Depth (m)	Description	Vs (m/s)
0.0 - 6.5	Mainly silty sands	170
6.5 - 30.0	Riccarton Gravels	280 - 584

A.2.4 Site CACS - Christchurch Canterbury Aero Club The site-characterization data used in this study to characterize the site CACS was obtained from Wotherspoon et al. (2015). Figure A.11 shows the location of the site-characterization data available (including V_S, HVSR, SPT, and borehole data) relative to the strong-motion station (represented by a yellow circle). In particular, the V_S profile used in this study corresponds to the linear array SW1. Borehole BH1 (which had a depth of 15.2 m) shows gravels from the surface to the bottom. Groundwater was not encountered in borehole BH1 and regional maps (Van Ballegooy et al., 2014; Westerhoff et al., 2018) suggest a long-term average water table between 0.5 to 7.0 m. A value of 7.0 m was chosen as representative for this site.

Table A.6 provides an interpreted stratigraphy of the site CACS down to 30 m depth, based on the available site-characterization data.

Figure A.11. Location of the site investigation at the site CACS (Wotherspoon et al. 2015).

Table A.6. CACS stratigraphy down to 30 m depth.

Depth (m)	Description	Vs (m/s)
0.0 - 30.0	Gravels	282 - 600

A.3 Simulation profiles

Figures A.12, A.13, A.14, and A.15 show the LF and HF simulation V_S, the NZVM V_S, and the site-specific V_S profiles, for the sites PRPC, CMHS, RHSC, and CACS, respectively.

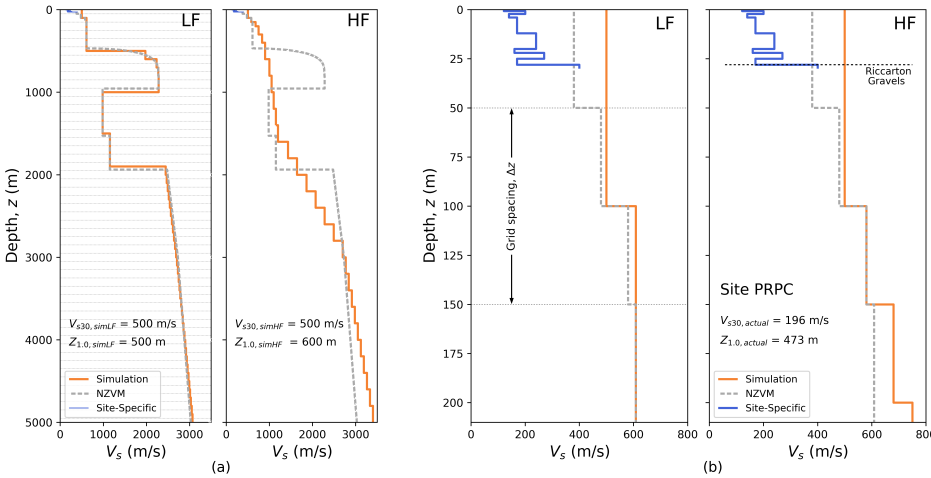

Figure A.12. Site-specific, NZVM, and LF and HF simulation V_S profiles at PRPC. The horizontal gray lines in the LF profile represent the grid distribution considered in the LF simulation.

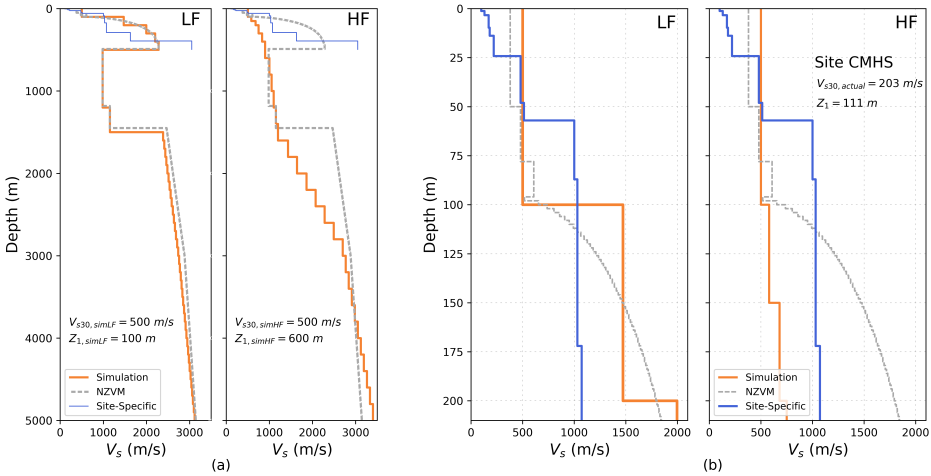

Figure A.13. Site-specific, NZVM, and LF and HF simulation V_S profiles at CMHS. The horizontal gray lines in the LF profile represent the grid distribution considered in the LF simulation.

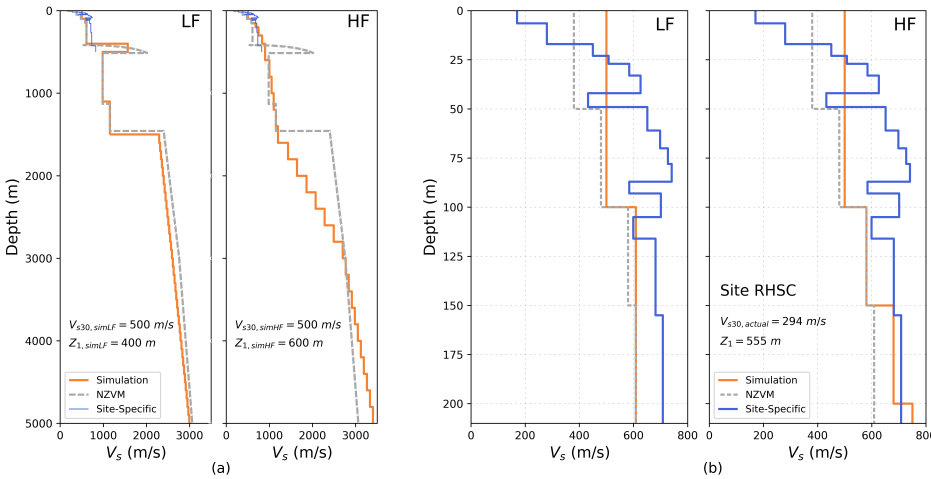

Figure A.14. Site-specific, NZVM, and LF and HF simulation V_S profiles at RHSC. The horizontal gray lines in the LF profile represent the grid distribution considered in the LF simulation.

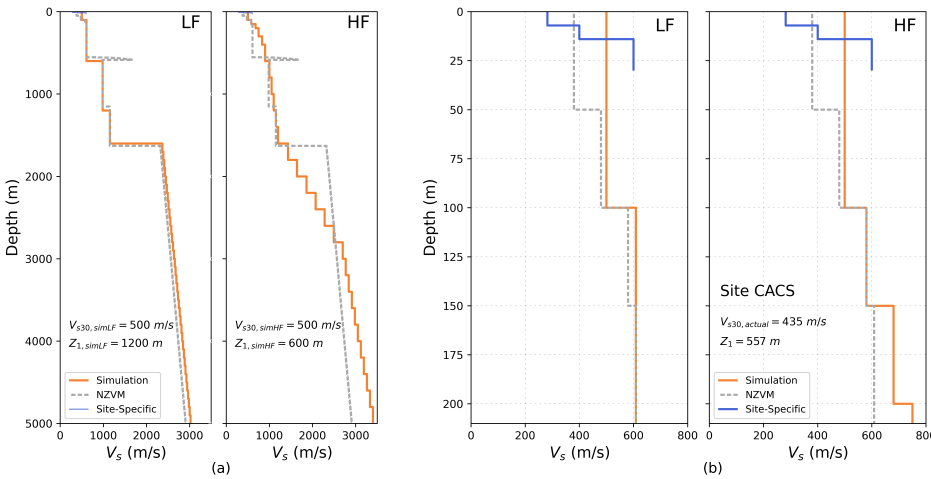

Figure A.15. Site-specific, NZVM, and LF and HF simulation V_S profiles at CACS. The horizontal gray lines in the LF profile represent the grid distribution considered in the LF simulation.

B Electronic Supplement B: Further description of methodological aspects

B.1 Application of the site factor

Figure B.1 describes the workflow for applying the site factor to the LF and HF simulation components and the subsequent filtering and merging in the time domain to produce the adjusted broadband acceleration time series, which accounts for shallow site effects.

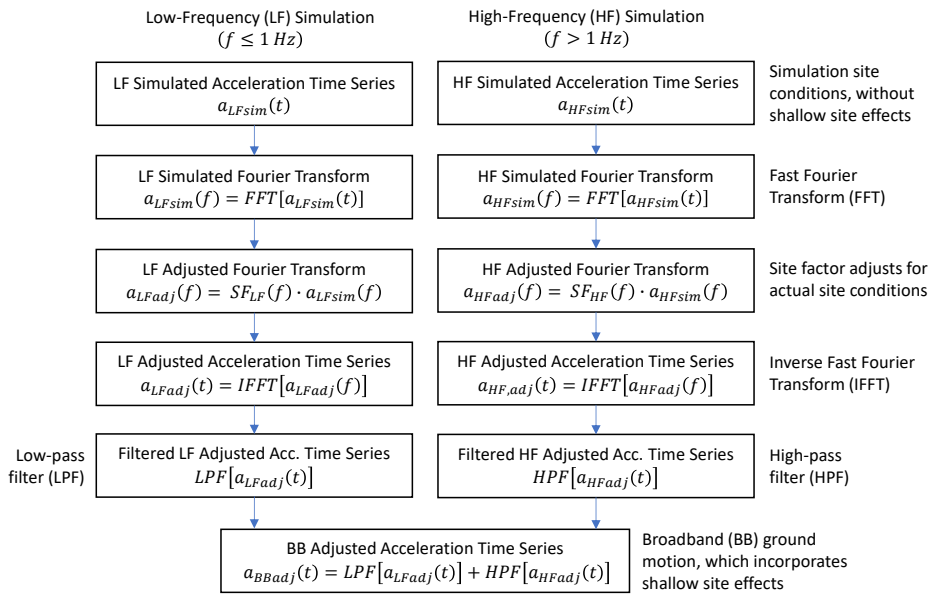

Figure B.1. Application of the site factor to the LF and HF simulation components.

Figure B.2 illustrates a modification of the previous workflow, where the site factor is only applied to the HF simulation component. This is the workflow used for applying Methods 1 and 2 in the "Comparison of the site amplification obtained with the five methods" section.

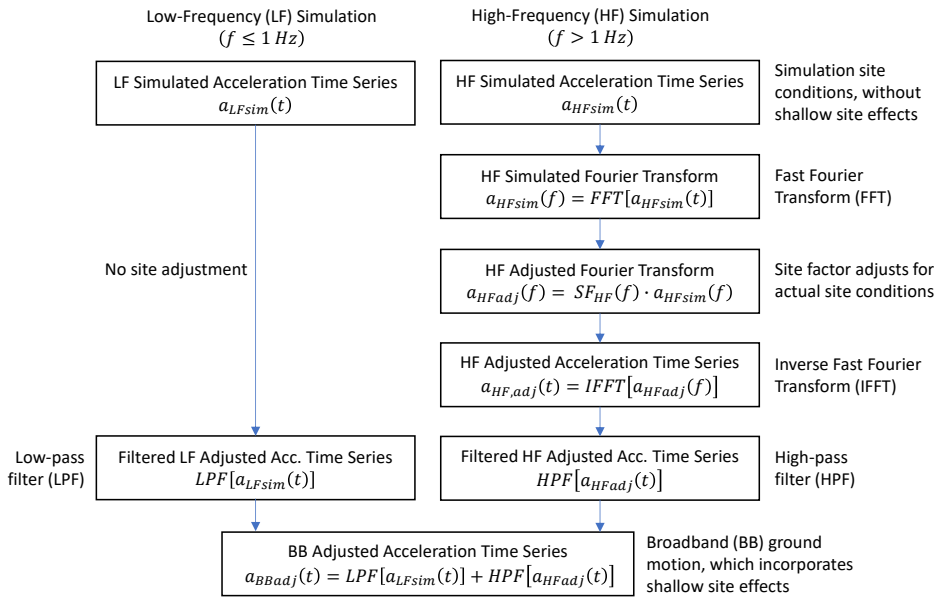

Figure B.2. Application of the site factor to the HF simulation component only.

B.2 GMMs used and considerations

This paper utilizes the ground-motion models CB14 (Campbell and Bozorgnia 2014), BSSA14 (Boore et al. 2014), BA18 (Bayless and Abrahamson 2019), and BCS19 (Bora et al. 2019), in addition to the site-response model SAG19 (Shi 2019, Ch. 4). Table B.1 indicates the limits of applicability of these models, in terms of V_{S30} range, and maximum $Z_{2.5}$ and $Z_{1.0}$ values. It should be noted that for the site PRPC, the $V_{S30,actual}$ value is slightly lower than the lower limit of the BCS19 model. In this case, a modified value of $V_{S30,actual} = 200$ was considered.

Table B.1. Limits of applicability of the different ground-motion and site-response models considered.

Model	V_{S30} (m/s)	$Z_{2.5,max}$ (m)	$Z_{1.0,max}$ (m)
CB14	150-1500	10000	-
BSSA14	150-1500	-	3000
BA18	180-1500	-	2000
BCS19	200-1000	-	-
SAG19	175-950	-	900

In addition, the SAG19 model has a range of PGA values that can be considered ($0.01g < PGA < 1.5g$), and a set of valid combination of V_{S30} and $Z_{1.0}$, which are indicated in Table B.2

Table B.2. Valid combinations of V_{S30} and $Z_{1.0}$ for the SAG19 model. For V_{S30} values greater than $V_{S30,min}$, a maximum value of $Z_{1.0} = Z_{1.0,max}$ is valid.

$V_{S30,min}$ (m/s)	$Z_{1.0,max}$ (m)
400	750
450	600
550	450
600	300
650	150
750	75
800	36
850	16

All the models consider a different reference V_{S30} condition for computing the site response. These values are presented in Table B.3.

The specific models considered to capture soil nonlinearity are referenced and described in Table B.4.

Table B.3. Reference V_{S30} associated with the models considered.

Model	Reference V_{S30} (m/s)
CB14	Variable with vibration period $400 \leq V_{S30} \leq 1086$
BSSA14	760
BA18	1000
BCS19	800
SAG19	1046

Table B.4. Nonlinear models considered in Method 1.

GMM	Nonlinear model	Type of nonlinear model	Site reponse analysis method considered	Spectral domain
CB14	Walling et al. (2008)	Analytical	1D equivalent linear	Response spectra
BSSA14	Seyhan and Stewart (2014)	Semi-empirical [Analytical component: Kamai et al. (2014)]	1D equivalent linear	Response spectra
BA18	Hashash et al. (2018)	Analytical	1D nonlinear	Fourier spectra
-	SAG19	Analytical	1D nonlinear	Fourier spectra

Each of the models considered use a different input IM_{rock} to compute the level of induced soil nonlinearity for a given ground motion:

- The CB14 model uses the PGA at a reference condition of V_{S30} = 1100 m/s.

- The BSSA14 model uses the PGA at a reference condition of V_{S30} = 760 m/s.

- The BA18 model uses the parameter I_R, which represents the PGA at rock outcrop. Since the model was developed in the Fourier spectral domain, Bayless and Abrahamson (2019) provide the following equation to estimate it: $ln(I_R) = 1.238 + 0.846 \cdot ln(EAS_{ref}(f = 5\,Hz))$, where EAS_{ref} is the orientation-independent horizontal-component Fourier amplitude spectrum for a reference condition V_{S30} = 760 m/s.

- The SAG19 model uses the PGA at a reference condition of V_{S30} = 1046 m/s.

Given that the regional ground-motion simulation is performed for a reference condition different from that used by the different models for IM_{rock}, an adjustment has to be performed. In this study, the PGA from the HF ground-motion simulation (PGA_{HF}), which is produced for a reference condition V_{S30} = 500 m/s, is adjusted to estimate IM_{rock} for the different models. In the case of the CB14, BSSA14 and SAG19 models, IM_{rock} is obtained according to

$$IM_{rock} = PGA_{HF} \cdot \frac{\exp(f_L(T = 0\,s, V_{S30,refNLmodel}))}{\exp(f_L(T = 0\,s, V_{S30,simHF}))} \tag{B.1}$$

which represents a linear adjustment, where $V_{S30,simHF}$ = 500 m/s and $V_{S30,refNLmodel}$ is equal to 1100 m/s for the CB14 model, 760 m/s for the BSSA14 model, and 1046 m/s for the SAG19 model. Even though the SAG19 model used in this paper for the computation of the site factor SF_1 was developed in the Fourier spectral domain, there is a version of this model derived in the response spectral domain, which is used for this linear adjustment. Since the maximum V_{S30} value that this model can manage is 950 m/s, the linear adjustment is performed for this reference condition instead of 1046 m/s. Also, since the minimum PGA that this model can use is 0.01 g, this value is considered for estimating f_L.

Since the BA18 model was developed in the Fourier spectral domain, the linear adjustment is slightly different. From the definition of I_R, it can be shown that the linear adjustment required is

$$IM_{rock} = PGA_{HF} \cdot \left[\frac{\exp(f_L(f = 5Hz, V_{S30,refNLmodel}))}{\exp(f_L(f = 5Hz, V_{S30,simHF}))} \right]^{0.846} \quad \text{(B.2)}$$

where $V_{S30,refNLmodel}$ = 760 m/s.

Tables B.5 and B.6 show the PGA_{HF} directly obtained from the HF simulations, and the resulting IM_{rock} values for the different models, for the low- and high-amplitude motions, respectively. Given that $V_{S30,refNLmodel} > V_{S30,simHF}$, the IM_{rock} values are lower than PGA_{HF} as a result of removing the linear site effects produced between these two conditions.

Table B.5. HF PGA and associated IM_{rock} values for the different models considered, for the low-amplitude motion.

Site	PGA_{HF} (g)	IM_{rock} (g)			
		CB14	BSSA14	BA18	SAG19
	V_{S30}=500 m/s	PGA(V_{S30}=1100 m/s)	PGA(V_{S30}=760 m/s)	I_R	PGA(V_{S30}=950 m/s)
PRPC	0.024	0.019	0.019	0.021	0.016
CMHS	0.036	0.028	0.028	0.030	0.023
RHSC	0.011	0.008	0.008	0.009	0.010
CACS	0.023	0.018	0.018	0.020	0.015

B.3 Definition of the reference condition in Method 4

This supplemental section provides further clarification on the selection of the reference condition in Method 4, particularly regarding the definition of the reference soil density.

As explained in the “Method 4 - 1D transfer function-based amplification” section, Method 4 involves performing two linear site response analyses (using two different

Table B.6. HF PGA and associated IM_{rock} values for the different models considered, for the high-amplitude motion.

Site	PGA_{HF} (g)	IM_{rock} (g)			
		CB14	BSSA14	BA18	SAG19
	V_{S30} = 500 m/s	PGA(V_{S30}=1100 m/s)	PGA(V_{S30}=760 m/s)	I_R	PGA(V_{S30}=950 m/s)
PRPC	0.46	0.36	0.36	0.39	0.30
CMHS	0.69	0.54	0.54	0.58	0.46
RHSC	0.30	0.23	0.23	0.25	0.20
CACS	0.25	0.20	0.19	0.21	0.16

approaches) relative to a common reference condition. This is illustrated in Equation 13 (rewritten below), where the numerator represents the linear analysis using the actual site properties and the theoretical 1D transfer function ($TF_{SH1D,actual}$), and the denominator represents the linear analysis using the simulation site properties and the SRI method ($TF_{SRI,sim}$).

$$SF_{4,L}(f) = \frac{|TF_{SH1D,actual}(V_{S,actual}, \rho_{actual}, D_{min,actual})|}{\sqrt{\frac{\rho_R V_{S,R}}{\bar{\rho}_{sim}\bar{V}_{S,sim}}} \cdot \exp[-\pi f \Delta\kappa_{0,sim}]} \tag{B.3}$$

As shown in Figure 7(a), the reference condition (elastic half-space) is defined at a certain depth where the actual and simulation V_S values match. The reference soil density, ρ_R, used in the denominator of the above equation, is obtained from the ρ model utilized in the regional simulations at the reference depth of 100 m considered in this study (e.g., ρ_R=1.81 T/m^3 for the HF simulation). This is done for consistency with the simulation methodology, since the purpose of this SRI-based transfer function is to remove the shallow site effects introduced by the simulation. Regarding the ρ_{actual} values considered in the numerator of the above equation, these were estimated using a V_S-based correlation (Rix et al. 2019), which results in a different value at the reference depth (e.g., 2.19 T/m^3 for the site PRPC) from that considered in the simulation. This raises the question of which of the two ρ values should be considered at the half-space of the site-response model representative of the actual site condition ($TF_{SH1D,actual}$). Considering that the two previously described site response analyses are performed using different approaches, in this study the V_S-based ρ value (e.g., 2.19 T/m^3 for the site PRPC) was chosen as reference for $TF_{SH1D,actual}$, for internal consistency within this approach.

C Electronic Supplement C: Additional results

C.1 Method 1

Figures C.1 to C.8 illustrate the determination of the linear and (full) site factors in Method 1, for the four sites considered. In addition to the CB14, BSSA14, and BA18 models, this section also provides results for the BCS19 and SAG19 models. In the case of the BCS19 model, only $SF_{1,L}$ is presented since the model does not include a nonlinear term. Unlike the other models, SAG19 was developed purely analytically through multiple 1D site-response analyses. This model, available in the Python library PySeismoSoil (Jsh9 2023), provides the site response amplification up to 20 Hz, thus, the site factor is extrapolated for f>20 Hz using a constant value (similar to Shi 2019).

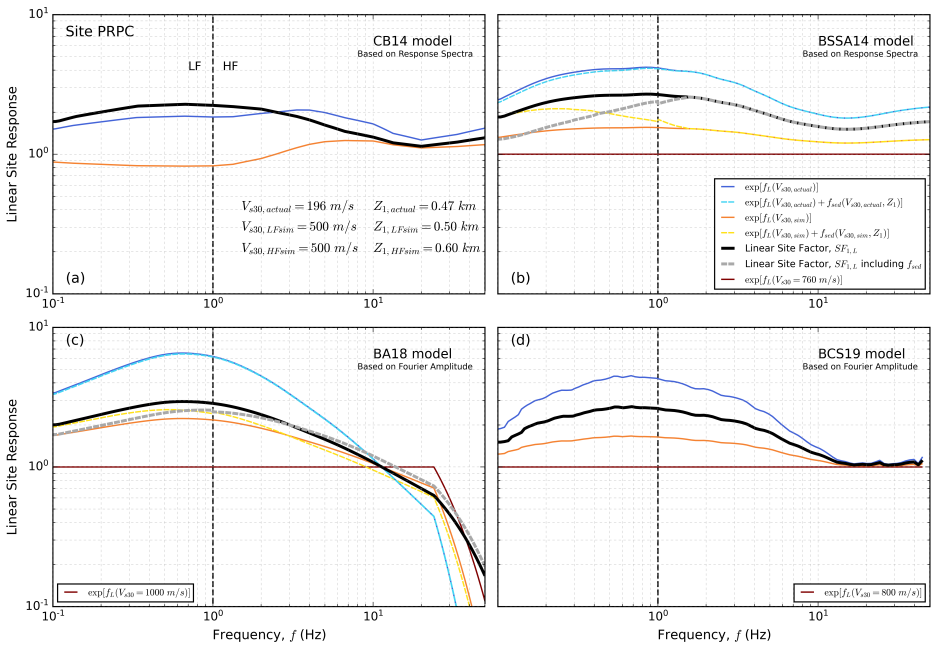

Figure C.1. Determination of the linear site factor in Method 1 for the site PRPC, for the GMMs (a) CB14, (b) BSSA14, (c) BA18, and (d) BCS19.

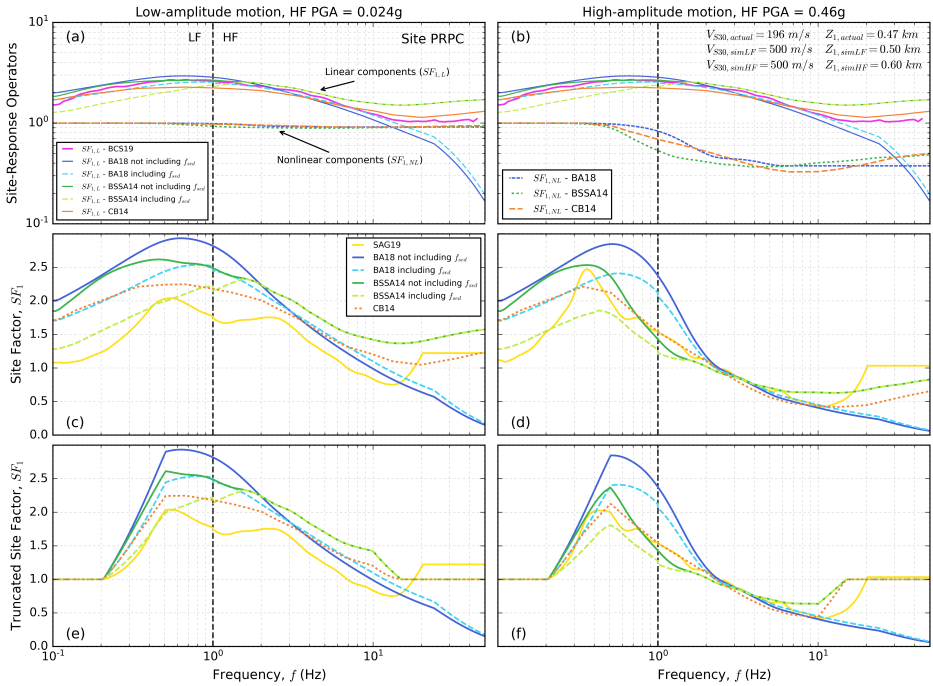

Figure C.2. Site factors obtained for the site PRPC using Method 1 and different models. (a) and (b) show the linear and nonlinear components for the low-amplitude and high-amplitude motion, respectively; (c) and (d) present the resulting site factors without any truncations; and (e) and (f) show the site factors with LF and HF truncations.

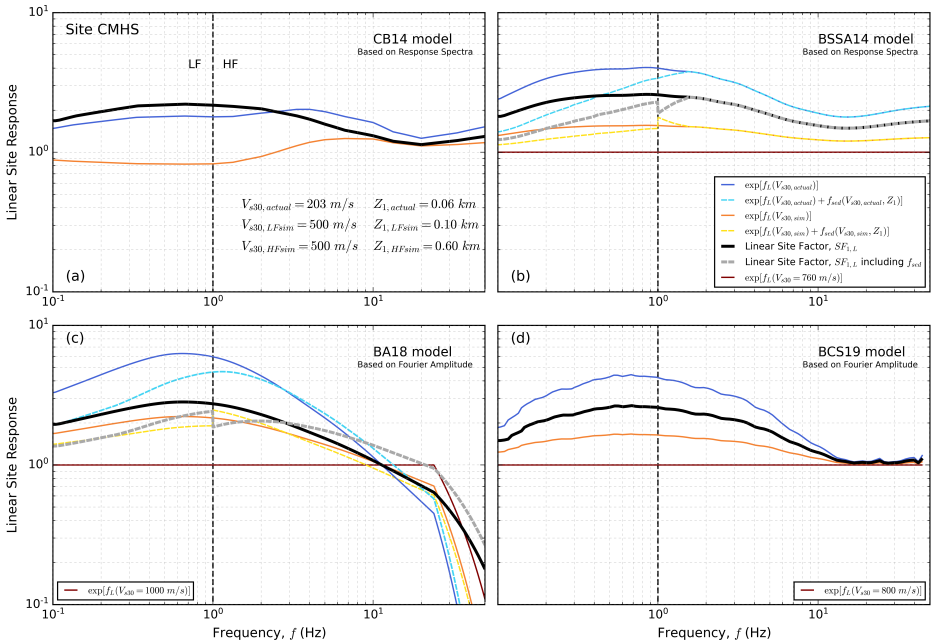

Figure C.3. Determination of the linear site factor in Method 1 for the site CMHS, for the GMMs (a) CB14, (b) BSSA14, (c) BA18, and (d) BCS19.

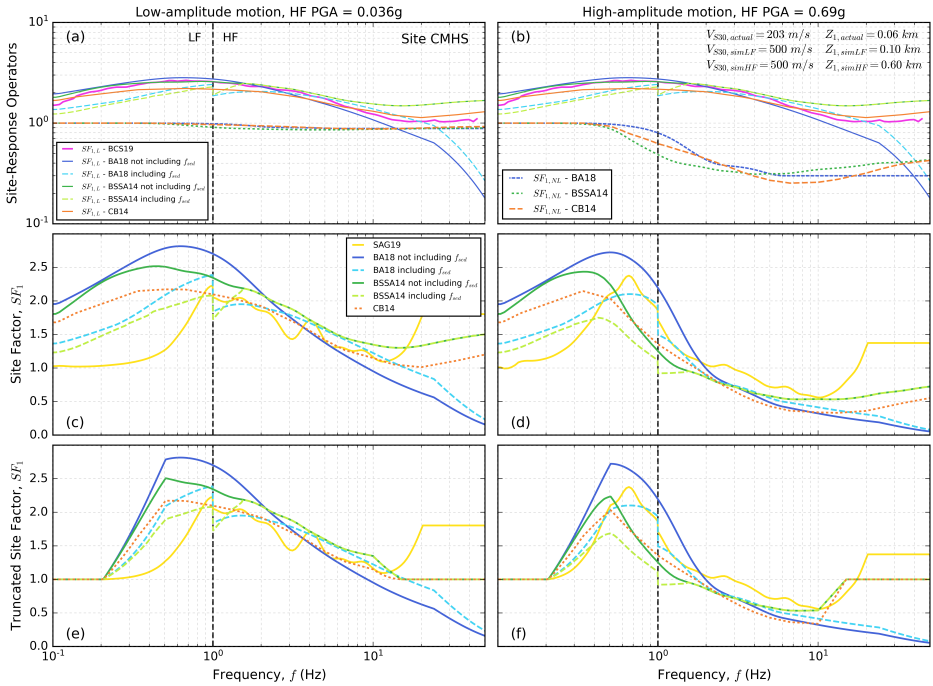

Figure C.4. Site factors obtained for the site CMHS using Method 1 and different models. (a) and (b) show the linear and nonlinear components for the low-amplitude and high-amplitude motion, respectively; (c) and (d) present the resulting site factors without any truncations; and (e) and (f) show the site factors with LF and HF truncations.

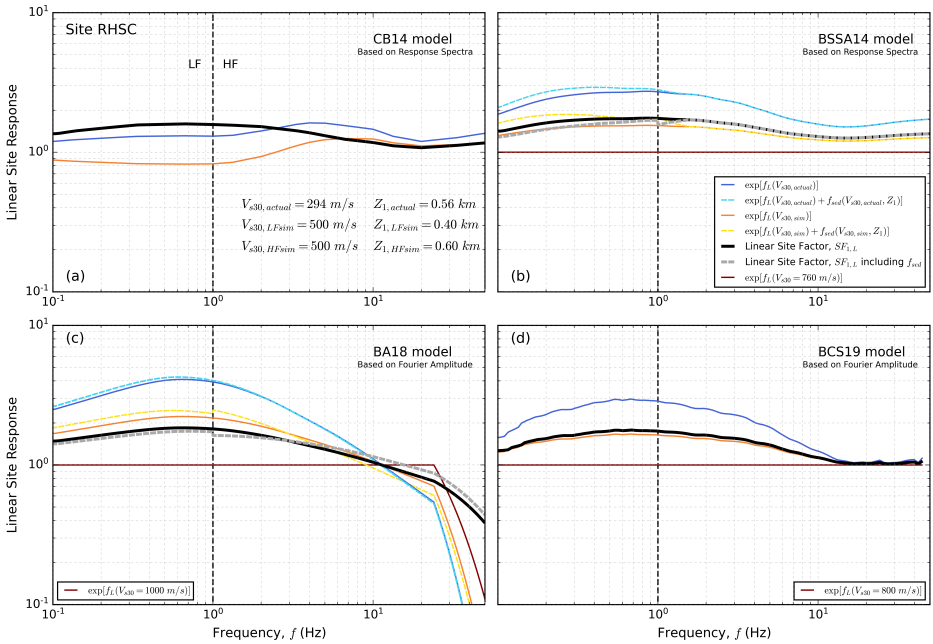

Figure C.5. Determination of the linear site factor in Method 1 for the site RHSC, for the GMMs (a) CB14, (b) BSSA14, (c) BA18, and (d) BCS19.

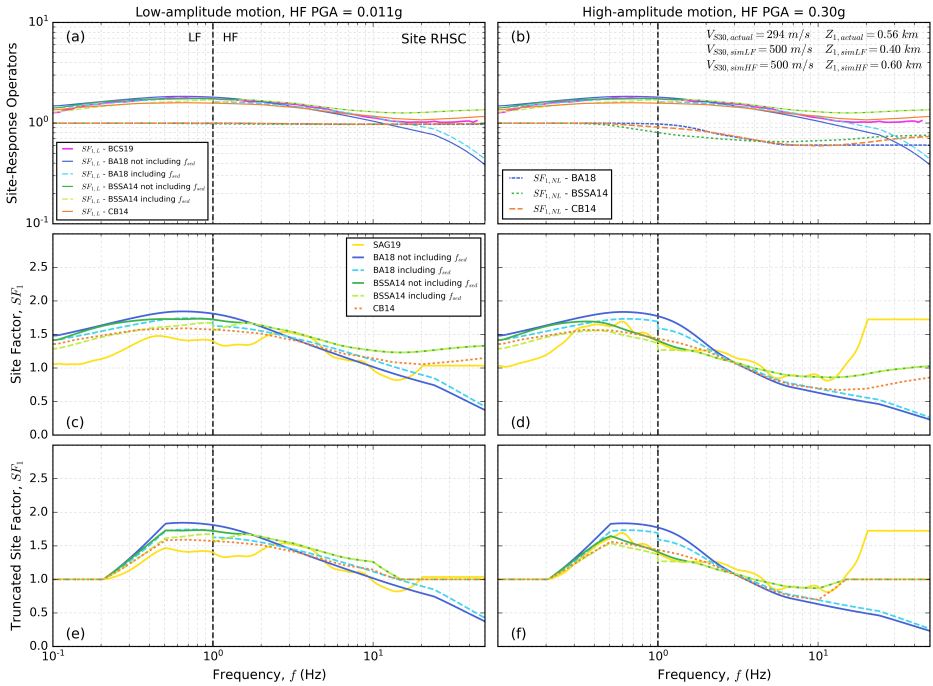

Figure C.6. Site factors obtained for the site RHSC using Method 1 and different models. (a) and (b) show the linear and nonlinear components for the low-amplitude and high-amplitude motion, respectively; (c) and (d) present the resulting site factors without any truncations; and (e) and (f) show the site factors with LF and HF truncations.

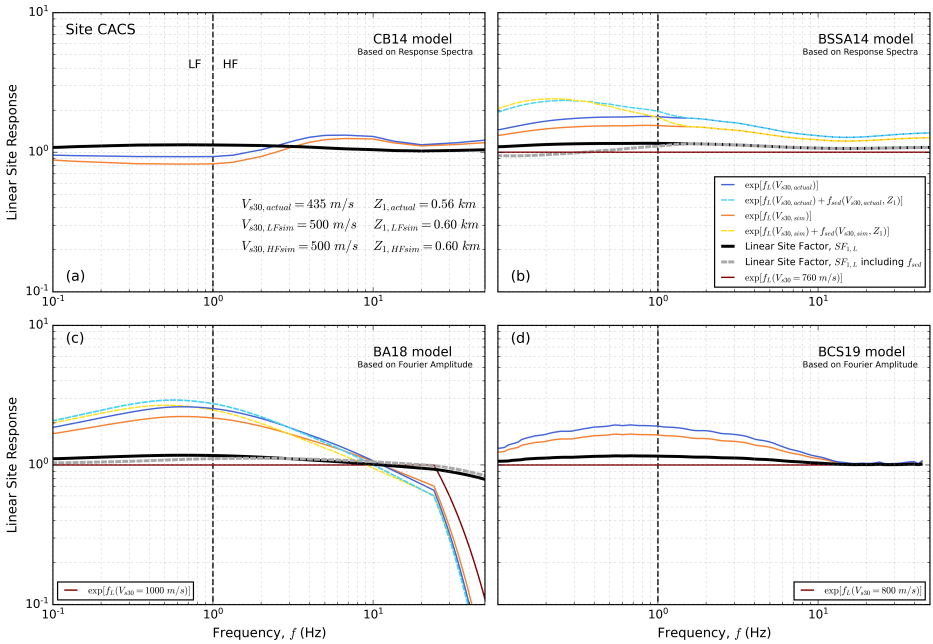

Figure C.7. Determination of the linear site factor in Method 1 for the site CACS, for the GMMs (a) CB14, (b) BSSA14, (c) BA18, and (d) BCS19.

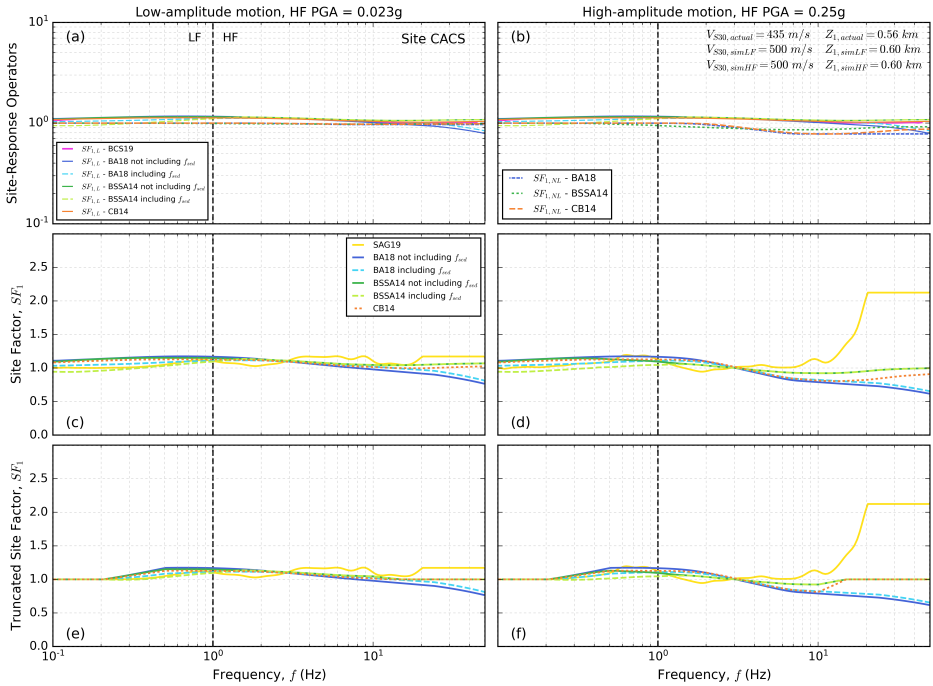

Figure C.8. Site factors obtained for the site CACS using Method 1 and different models. (a) and (b) show the linear and nonlinear components for the low-amplitude and high-amplitude motion, respectively; (c) and (d) present the resulting site factors without any truncations; and (e) and (f) show the site factors with LF and HF truncations.

C.2 Effect of f_{sed} on $SF_{1,L}$

As observed in Figures C.1, C.3, C.5, and C.7, the linear site factor $SF_{1,L}$ is modified when the f_{sed} terms ($f_{sed,actual}$ and $f_{sed,sim}$) are included (in the case of the BA18 and BSSA14 models). In the following, this modification is explained and discussed, using the BSSA14 model (Boore et al. 2014) as reference.

The f_{sed} term in the BSSA14 model, which is called $F_{\delta z_1}$ in Boore et al. (2014), only affects vibration periods $T \geq 0.65$ s, or equivalently, frequencies $f \leq 1.54$ Hz (i.e., mainly the LF range is affected). This term is included in the BSSA14 model to account for the effect of basin depth on the ground-motion amplitude. For a given V_{S30} value, a representative $Z_{1.0}$ in the region of interest can be estimated through empirical correlations. Then, the difference ($\delta Z_{1.0}$) between the site-specific $Z_{1.0}$ value and the V_{S30}-based $Z_{1.0}$ estimate is used to compute f_{sed}. In other words, f_{sed} is an adjustment that depends on how much the site-specific $Z_{1.0}$ value departs from the expected value for a certain region given a V_{S30}. This procedure is illustrated in Figure C.9 for the site PRPC, for both the actual and LF simulation conditions.

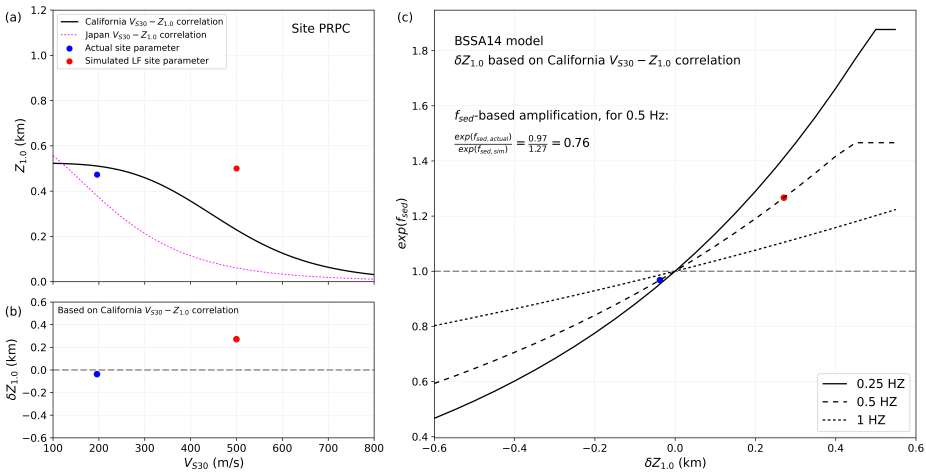

Figure C.9. Illustration of the $Z_{1.0}$-based f_{sed} adjustment in the BSSA14 model for the site PRPC. (a) Empirical $V_{S30} - Z_{1.0}$ relationship for California and Japan. (b) δz_1 for the actual and LF simulation site conditions, using the California relationship. (c) f_{sed} values for different frequencies, and resulting amplification for f = 0.5 Hz.

Figure C.9(a) shows the empirical $Z_{1.0} - V_{S30}$ relationships used in the BSSA14 model for California and Japan, along with the actual and simulation values for PRPC. Figure C.9(b) presents the $\delta Z_{1.0}$ values for the actual and simulation conditions, based on

the relationship for California. In this case, the actual $\delta Z_{1.0}$ is very close to zero ($\delta Z_{1.0}$ = -0.038 km), which indicates that for the $V_{S30,actual}$ value associated with PRPC, $Z_{1.0,actual}$ is very similar to the expected value in California. On the other hand, the simulation $\delta Z_{1.0}$ is considerably higher ($\delta Z_{1.0}$ = 0.27 km) than the expected value in California for $V_{S30,sim}$ = 500 m/s, which can be understood in light of the issue discussed in the "Host-to-target correction issue" section (i.e., the average V_S profile for California for V_{S30} = 500 m/s tends to be stiffer at depth than the simulation V_S profile, resulting in a higher $Z_{1.0}$ value for the simulation profile). Figure C.9(c) shows how $\delta Z_{1.0}$ is mapped into $exp(f_{sed})$ for different frequencies. In the case of f = 0.50 Hz, it is shown that $exp(f_{sed})$ is very close to 1 (i.e., no adjustment) for the actual condition [$exp(f_{sed,actual})$]. For the simulation condition, however, $exp(f_{sed,sim})$ = 1.27, meaning that the ground-motion needs to be amplified at f = 0.50 Hz to account for the fact that the simulation profile is characterized by a higher value of $Z_{1.0}$ than expected.

The effect of $exp(f_{sed,actual})$ and $exp(f_{sed,sim})$ on $SF_{1,L}$ is a multiplicative factor computed as $exp(f_{sed,actual} - f_{sed,sim})$. As shown in Figure C.9(c), in the case of PRPC, this results in a factor of 0.78, meaning that the net effect of including the f_{sed} terms is a reduction in $SF_{1,L}$ at f = 0.50 Hz. As it can be appreciated from Figure C.9(c), this adjustment is less significant for higher frequencies (e.g., 1 Hz).

Figure C.10 presents the f_{sed} terms for the four sites considered. The figure shows that the site CMHS is the only case where $\delta Z_{1.0}$ is lower than zero for the simulation condition, and where $\delta Z_{1.0}$ is significantly lower than zero for the actual condition, illustrating that this is a particularly shallow site.

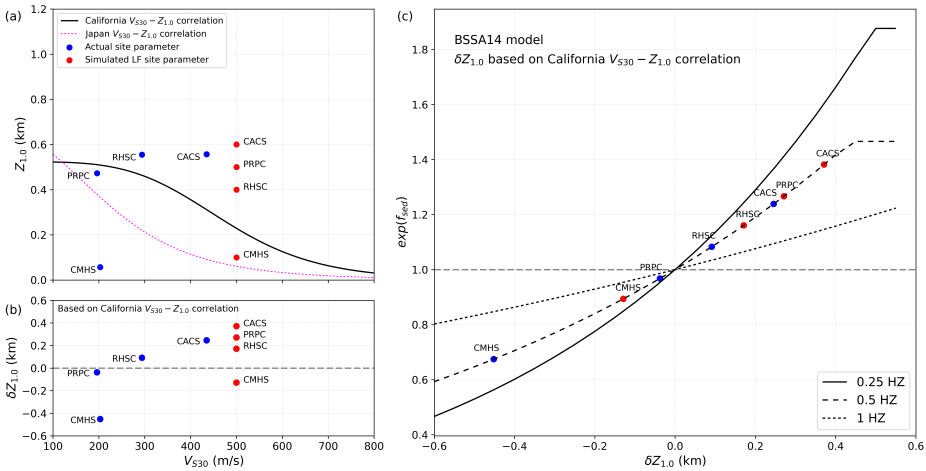

Figure C.10. Illustration of the $Z_{1.0}$-based f_{sed} adjustment in the BSSA14 model for the four sites considered. (a) Empirical $V_{S30} - Z_{1.0}$ relationship for California and Japan. (b) δz_1 for the actual and LF simulation site conditions, using the California relationship. (c) Resulting f_{sed} values for different frequencies.

C.3 Method 2

Figure C.11 shows the reference adjustment proposed in Method 2 for the site PRPC and two GMMs: CB14 and BSSA14. As shown in Figure C.11a, the reference host profiles of the two GMMs are considerably different, resulting in different merging depths. Figure C.12 presents the corresponding site factor (SF_2), and compares them with those obtained with Method 1 (SF_1). For the CB14 model, the f_{sed} terms are not included in the computation of SF_1, and in the case of BSSA14, SF_1 is computed with and without the f_{sed} terms. When Method 2 is applied using the BSSA14 model, SF_1 is computed including $f_{sed,actual}$, but not $f_{sed,sim}$, as explained later. The results are shown with and without the LF and HF truncations previously considered in the "Method 1 - V_{S30}-based amplification" section. As illustrated in Figure C.12, once the HF truncation is applied, the net effect of the reference correction factor introduced by Method 2 is a significant reduction in the amplification implied by SF_1, mainly for $f<3$ Hz. However, at very low frequencies ($f<0.3$ Hz) the reduction in amplification generated by the simple application of the LF truncation to SF_1 is greater than that obtained by Method 2 (SF_2).

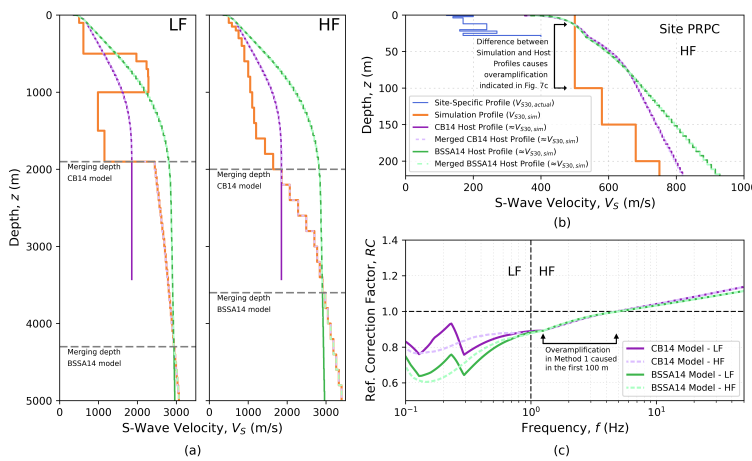

Figure C.11. Reference adjustment in Method 2 for the site PRPC. (a) LF and HF profiles, from 0 to 5000 m. (b) HF profiles from 0 to 220 m. (c) Resulting reference correction factors.

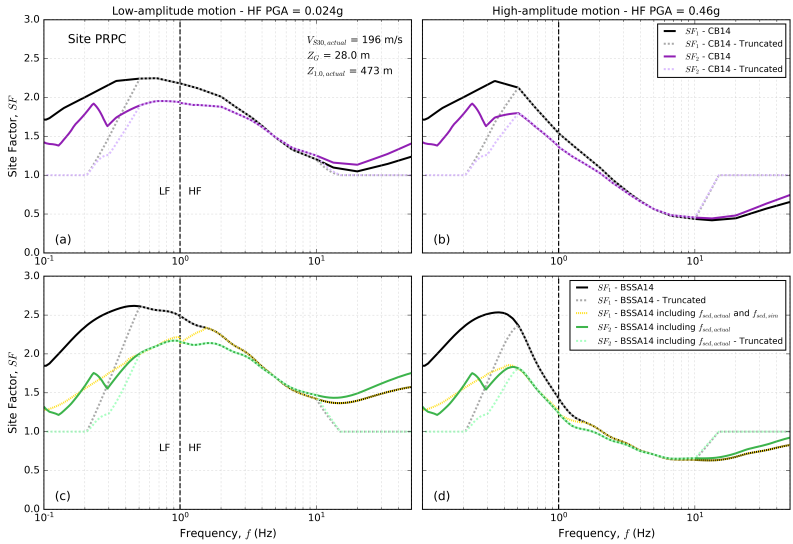

Figure C.12. Comparison between site factors obtained by Method 1 and Method 2 for the site PRPC. (a) CB14 model; for the low-amplitude motion and (b) the high-amplitude motion, (c) BSSA14 model; for the low-amplitude motion and (d) the high-amplitude motion.

In the case of the BSSA14 model, the application of Method 2 has a similar effect to the incorporation of the f_{sed} terms in Method 1 (Figures C.12c and C.12d). Supplemental Figure C.1 shows that the reduction of amplification in the latter case is driven by an increase in $exp[f_{site,sim}]$ when $f_{sed,sim}$ is included. Conceptually, this adjustment is similar to that performed with the reference correction factor (RC) in Method 2. The f_{sed} term in the BSSA14 model accounts for differences between the site $Z_{1.0}$ and the average (host) $Z_{1.0}$ value implicit in the model for a given V_{S30}. In this case, the simulation profile is characterized by a $Z_{1.0,sim}$ value that is larger than that implicit in the BSSA14 model for $V_{S30,sim}$, which results in an increase in $exp[f_{site,sim}]$ when $f_{sed,sim}$ is incorporated. This is further explained in the "Effect of f_{sed} on $SF_{1,L}$" section of Electronic Supplement C. The advantage of Method 2 is that the adjustment is site-specific (i.e., conducted for the particular simulation profile considered, instead of for its associated $Z_{1.0}$ value), resulting in lower amplification in the frequency range f=1-3 Hz for the site PRPC. However, the adjustment performed by Method 2 is only related to the simulation site response ($f_{S,sim}$) and does not have any influence in the actual site response ($f_{S,actual}$), which is the reason why the $f_{sed,actual}$ term was included in the computation of SF_2. Including this term is particularly relevant in the case of sites characterized by a $Z_{1.0,actual}$ value that departs significantly from the host $Z_{1.0}$ value for $V_{S30,actual}$, which is the case of the site CMHS,

as shown in the Supplemental Figure C.10 of the Electronic Supplement C. Another advantage of Method 2 is that it can be applied along with any GMM, whereas the type of V_{S30}-based f_{sed} adjustment described before is only available in some GMMs (e.g., BSSA14, BA18).

The following figures show the reference adjustment and the resulting site factors, for the the other three sites considered.

As observed in Figure C.14, in the case of the site CMHS, Method 2 along with the CB14 model produces an unrealistically large linear site factor in the LF range. This situation illustrates an issue that can occur at sites characterized by a $Z_{1.0,actual}$ value that significantly departs from the average $Z_{1.0}$ for a given $V_{S30,actual}$ (see Supplemental Figure C.10 in Electronic Supplement C). Since the correction introduced in Method 2 only acts over the simulation condition (represented by $V_{S30,sim}$), in these cases, the use of a GMM such as BSSA14, which allows for a correction of the actual condition (through a $V_{S30,actual}$-based $f_{sed,actual}$ adjustment) is preferred over a model like CB14, that does not have this feature.

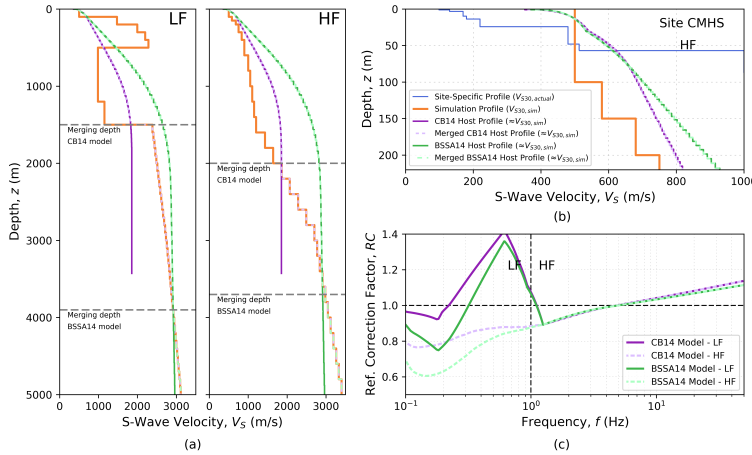

Figure C.13. Reference adjustment in Method 2 for the site CMHS. (a) LF and HF profiles, from 0 to 5000 m. (b) HF profiles from 0 to 220 m. (c) Resulting reference correction factors.

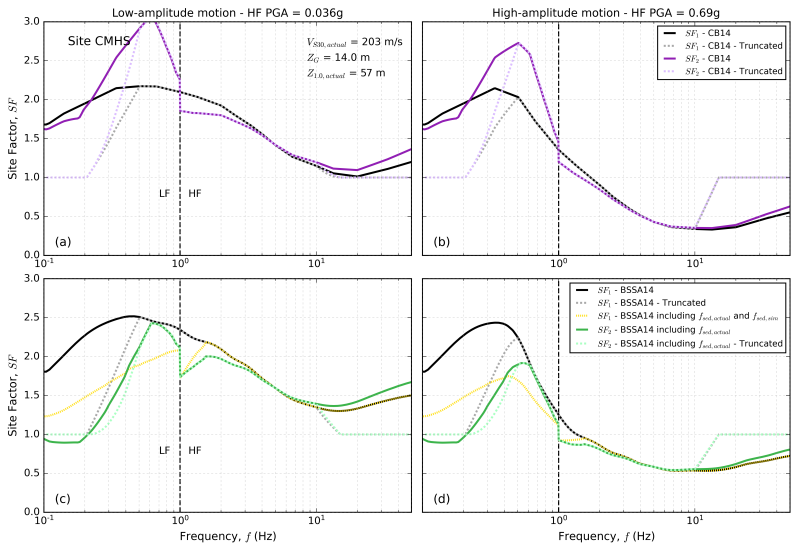

Figure C.14. Comparison between site factors obtained by Method 1 and Method 2 for the site CMHS. (a) CB14 model; for the low-amplitude motion and (b) the high-amplitude motion, (c) BSSA14 model; for the low-amplitude motion and (d) the high-amplitude motion.

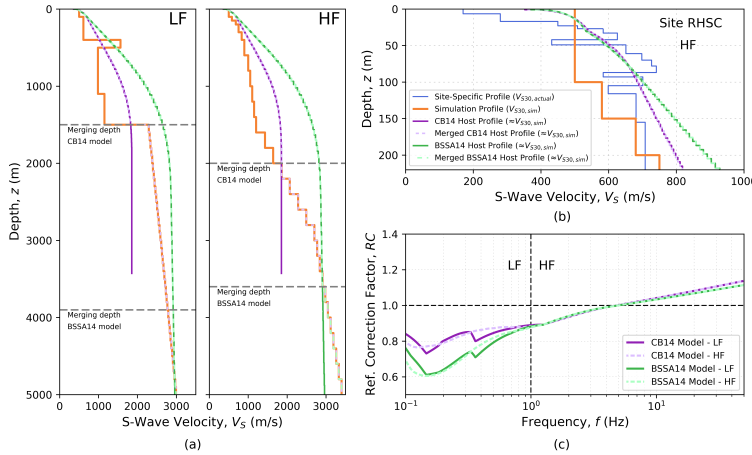

Figure C.15. Reference adjustment in Method 2 for the site RHSC. (a) LF and HF profiles, from 0 to 5000 m. (b) HF profiles from 0 to 220 m. (c) Resulting reference correction factors.

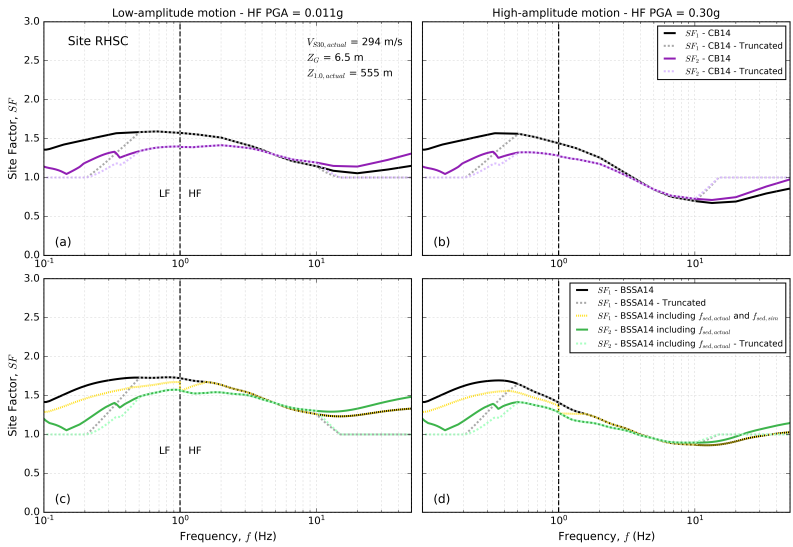

Figure C.16. Comparison between site factors obtained by Method 1 and Method 2 for the site RHSC. (a) CB14 model; for the low-amplitude motion and (b) the high-amplitude motion, (c) BSSA14 model; for the low-amplitude motion and (d) the high-amplitude motion.

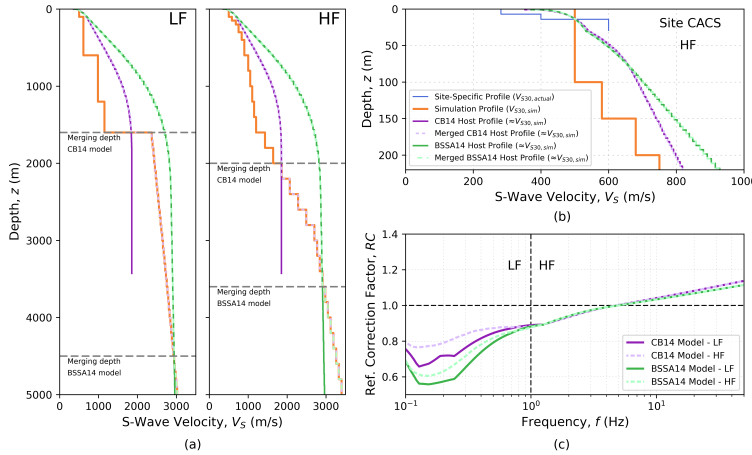

Figure C.17. Reference adjustment in Method 2 for the site CACS. (a) LF and HF profiles, from 0 to 5000 m. (b) HF profiles from 0 to 220 m. (c) Resulting reference correction factors.

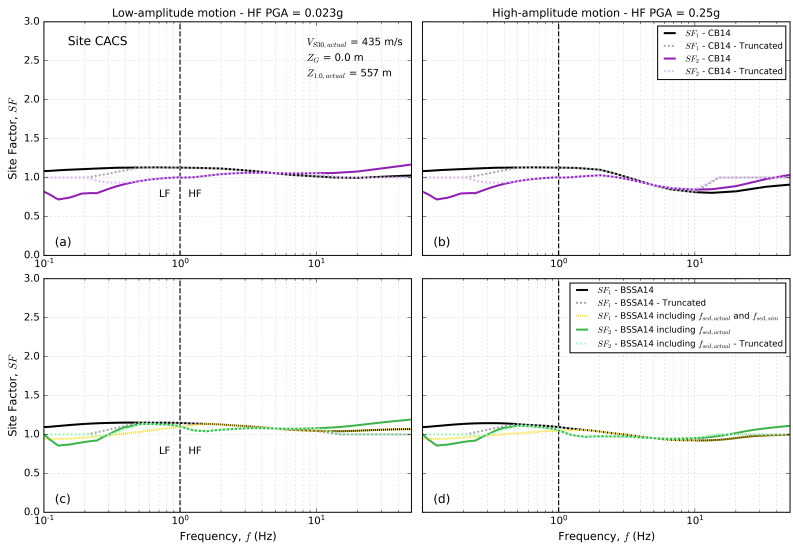

Figure C.18. Comparison between site factors obtained by Method 1 and Method 2 for the site CACS. (a) CB14 model; for the low-amplitude motion and (b) the high-amplitude motion, (c) BSSA14 model; for the low-amplitude motion and (d) the high-amplitude motion.

C.4 Method 3

Figures C.19 to C.26 show the V_S profiles used in Method 3 (and subsequently, in Method 4), and the resulting site factors, for the four sites considered.

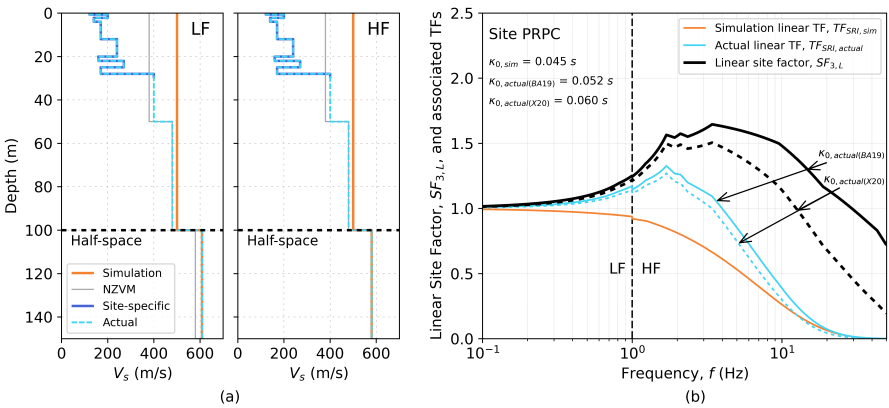

Figure C.19. (a) V_S profiles used in Methods 3 (and subsequently, in Method 4), for the site PRPC. (b) Resulting linear site factor.

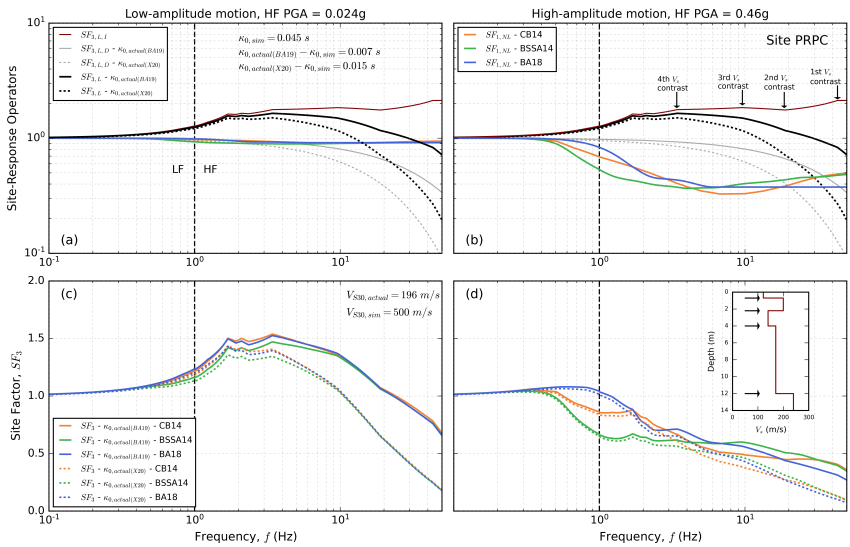

Figure C.20. (a) Site-response operators of Method 3 for the site PRPC considering the low-amplitude motion and (b) the high-amplitude motion. (c) Resulting site factors for the low-amplifude motion and (d) high-amplitude motion.

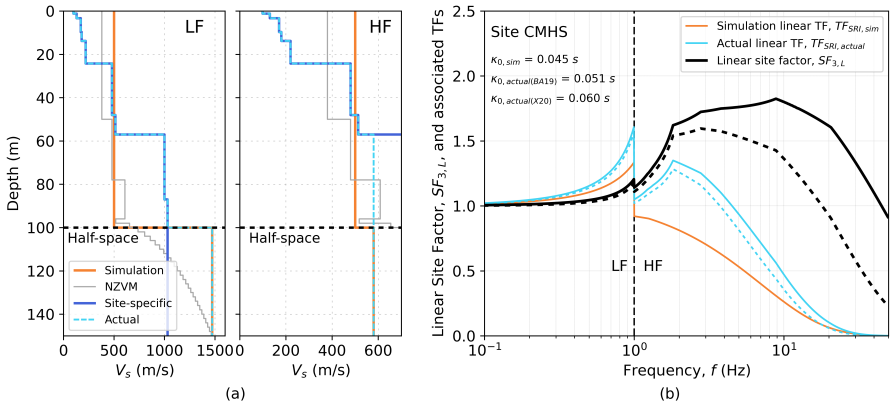

Figure C.21. (a) V_S profiles used in Methods 3 (and subsequently, in Method 4), for the site CMHS. (b) Resulting linear site factor.

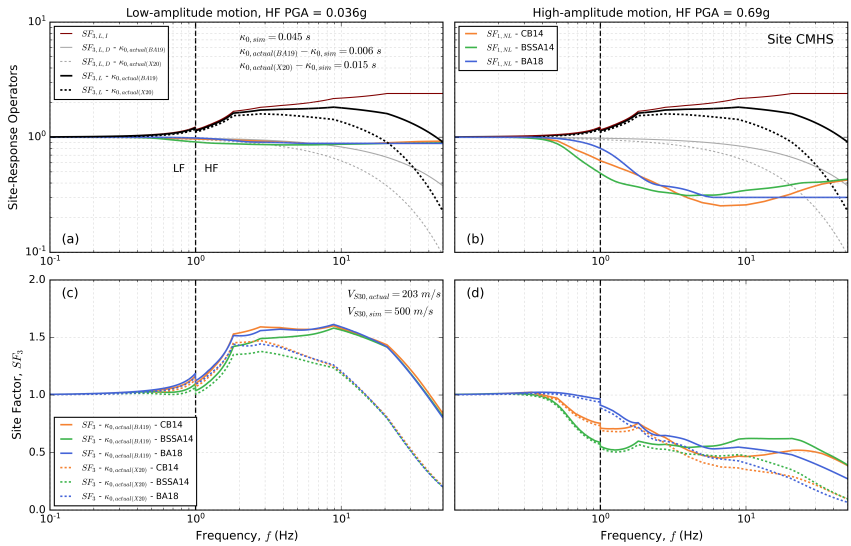

Figure C.22. (a) Site-response operators of Method 3 for the site CMHS considering the low-amplitude motion and (b) the high-amplitude motion. (c) Resulting site factors for the low-amplifude motion and (d) high-amplitude motion.

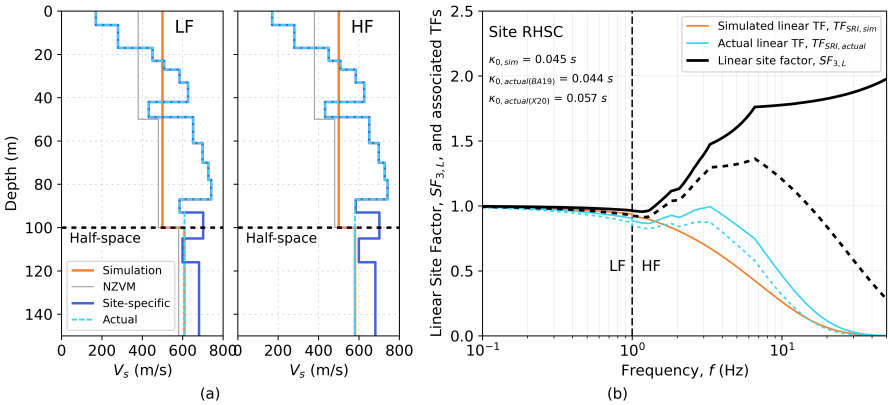

Figure C.23. (a) V_S profiles used in Methods 3 (and subsequently, in Method 4), for the site RHSC. (b) Resulting linear site factor.

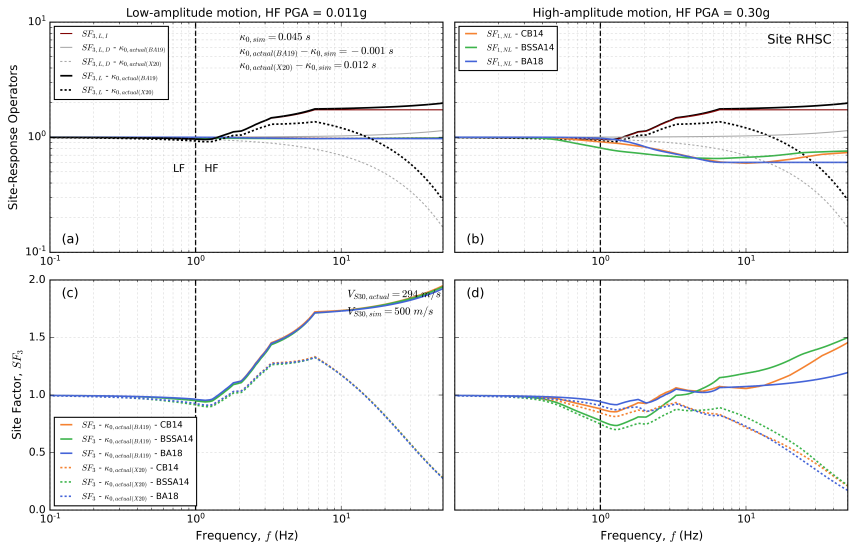

Figure C.24. (a) Site-response operators of Method 3 for the site RHSC considering the low-amplitude motion and (b) the high-amplitude motion. (c) Resulting site factors for the low-amplifude motion and (d) high-amplitude motion.

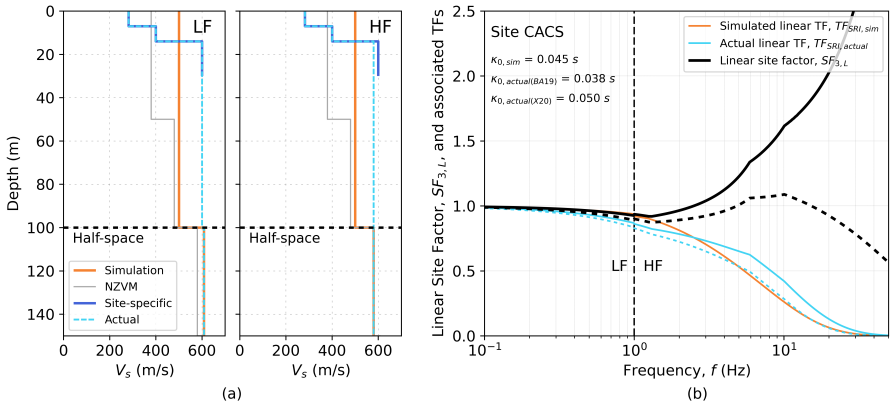

Figure C.25. (a) V_S profiles used in Methods 3 (and subsequently, in Method 4), for the site CACS. (b) Resulting linear site factor.

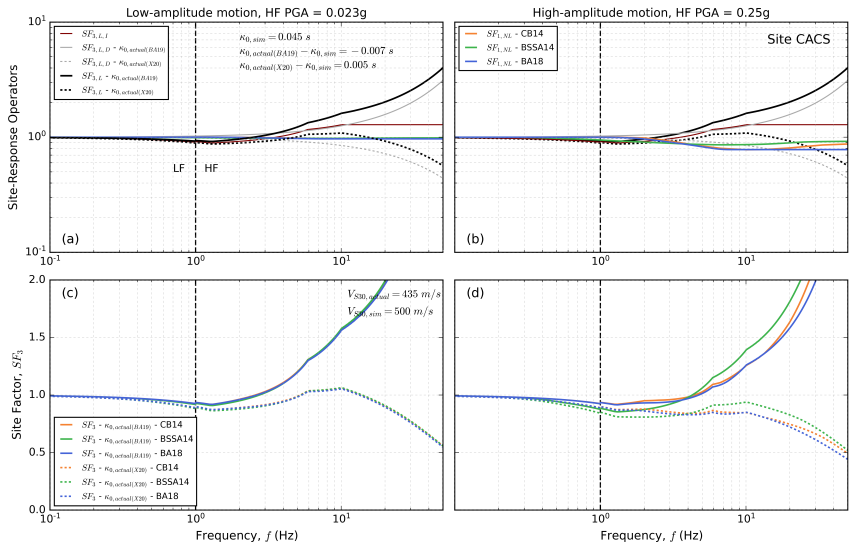

Figure C.26. (a) Site-response operators of Method 3 for the site CACS considering the low-amplitude motion and (b) the high-amplitude motion. (c) Resulting site factors for the low-amplifude motion and (d) high-amplitude motion.

C.5 Method 4

Figures C.27 to C.34 show the D_{min} profiles used in Method 4, and the resulting site factors, for the four sites considered.

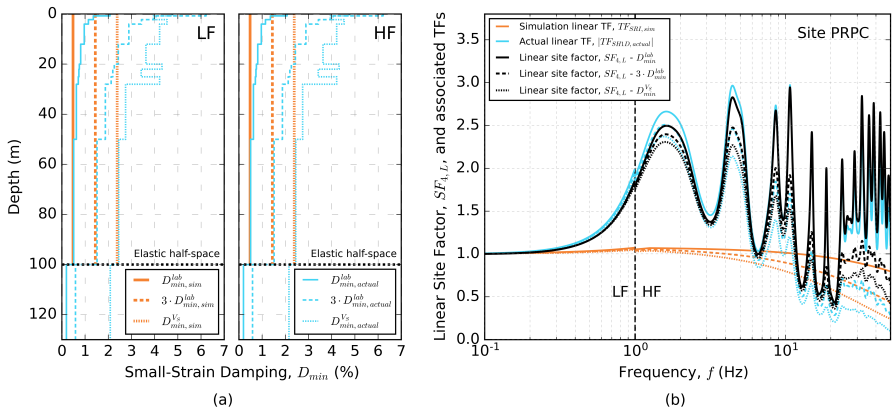

Figure C.27. (a) D_{min} profiles used in Method 4 for the site PRPC. (b) Resulting linear site factor from Method 4 for the site PPRC.

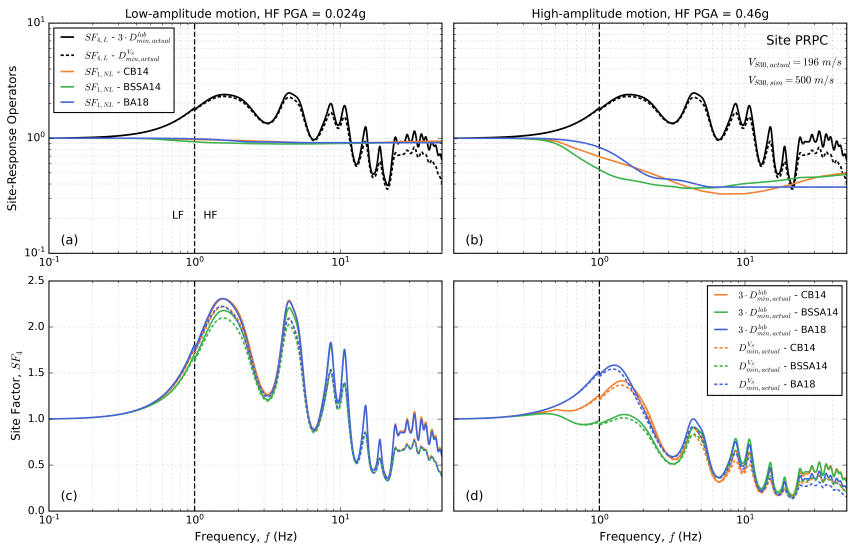

Figure C.28. (a) Site-response operators of Method 4 for the site PRPC considering the low-amplitude motion and (b) the high-amplitude motion. (c) Resulting site factors for the low-amplitude motion and (d) high-amplitude motion.

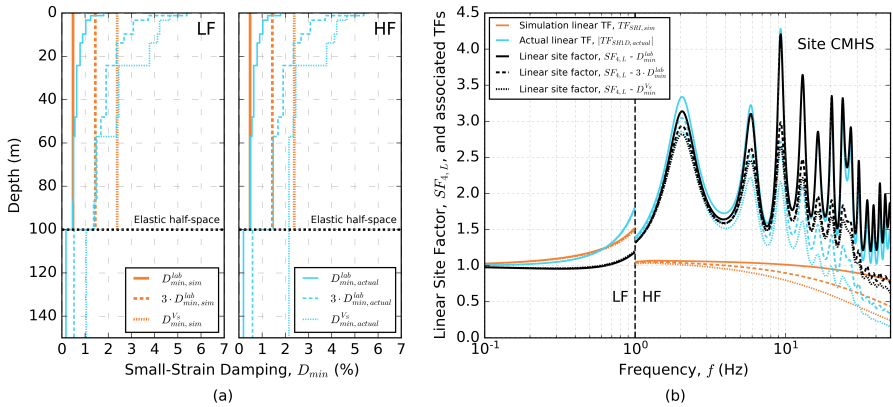

Figure C.29. (a) D_{min} profiles used in Method 4 for the site CMHS. (b) Resulting linear site factor from Method 4 for the site CMHS.

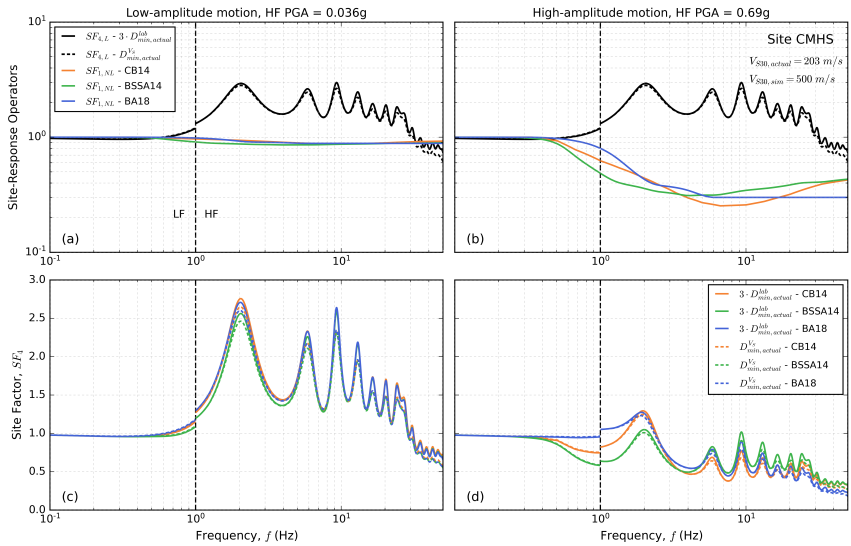

Figure C.30. (a) Site-response operators of Method 4 for the site CMHS considering the low-amplitude motion and (b) the high-amplitude motion. (c) Resulting site factors for the low-amplitude motion and (d) high-amplitude motion.

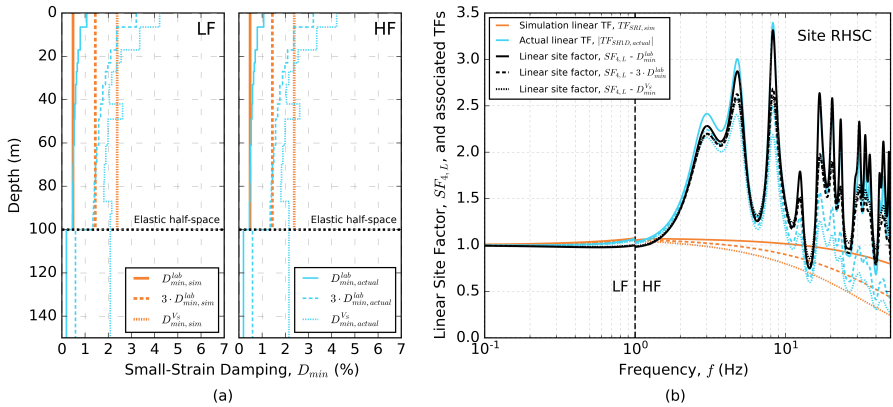

Figure C.31. (a) D_{min} profiles used in Method 4 for the site RHSC. (b) Resulting linear site factor from Method 4 for the site RHSC.

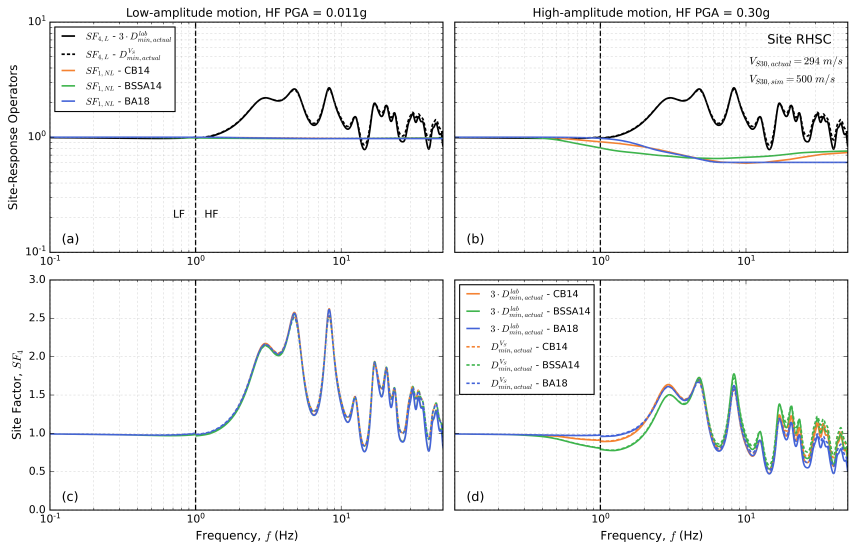

Figure C.32. (a) Site-response operators of Method 4 for the site RHSC considering the low-amplitude motion and (b) the high-amplitude motion. (c) Resulting site factors for the low-amplitude motion and (d) high-amplitude motion.

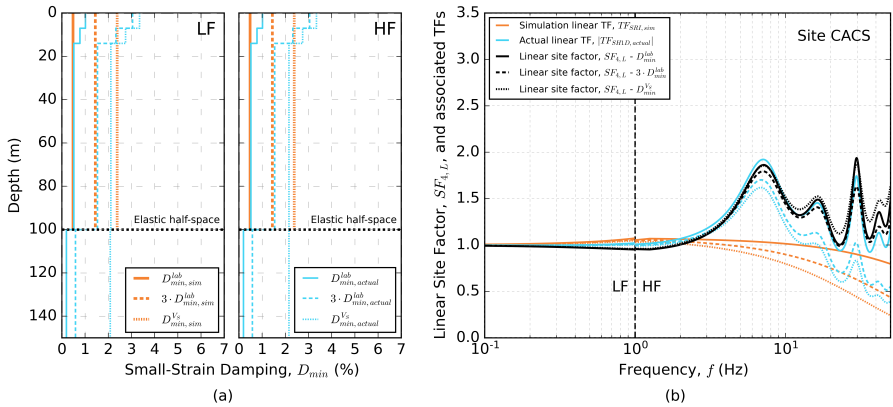

Figure C.33. (a) D_{min} profiles used in Method 4 for the site CACS. (b) Resulting linear site factor from Method 4 for the site CACS.

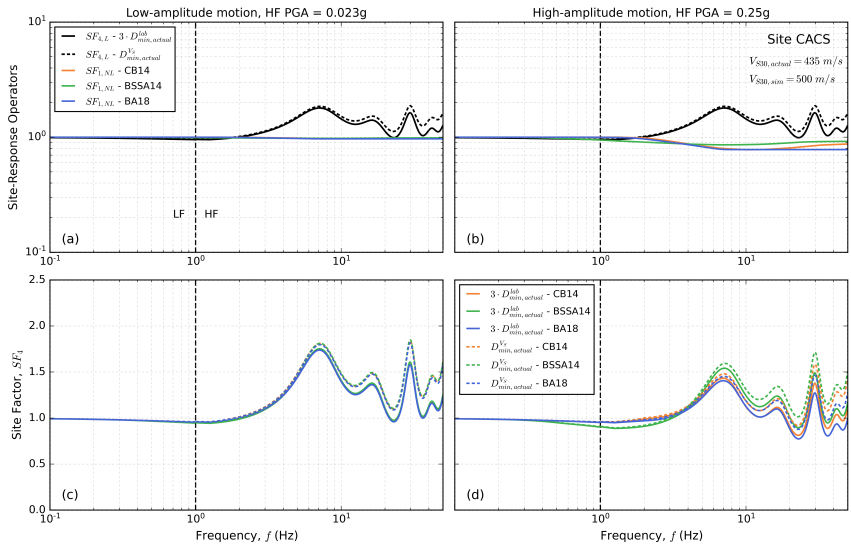

Figure C.34. (a) Site-response operators of Method 4 for the site CACS considering the low-amplitude motion and (b) the high-amplitude motion. (c) Resulting site factors for the low-amplitude motion and (d) high-amplitude motion.

C.6 Method 5

Figures C.35 to C.38 show the V_S profiles utilized in Method 5 and the resulting linear site factor $SF_{L,5}$ for the four sites considered.

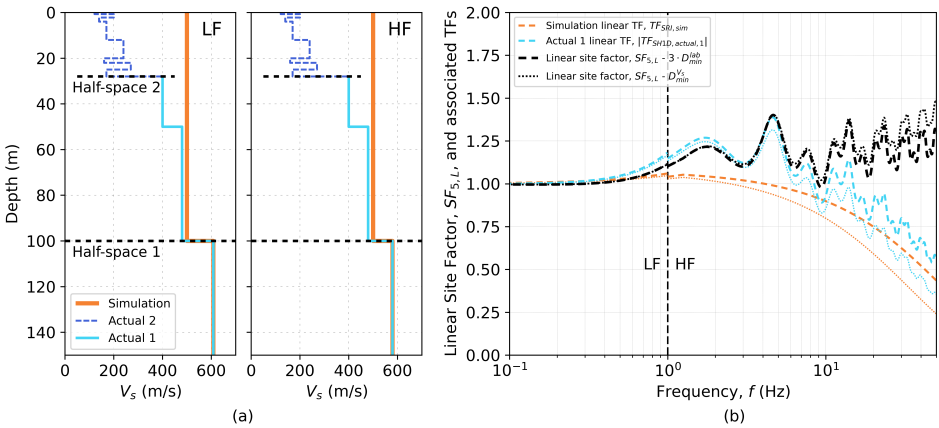

Figure C.35. (a) V_S profiles used in Methods 5 for the site PRPC, and (b) resulting linear site factor.

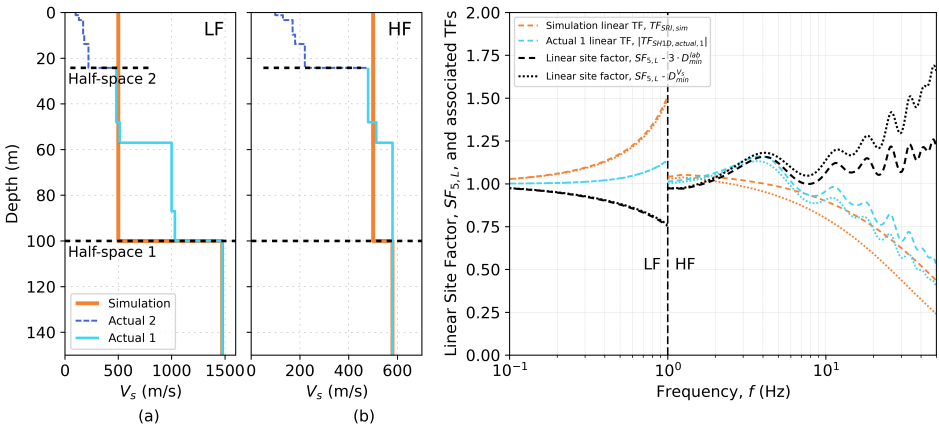

Figure C.36. (a) V_S profiles used in Methods 5 for the site CMHS, and (b) resulting linear site factor.

To investigate the impact of using different codes and models for 1D time-domain nonlinear site-response analysis in Method 5, four different analyses are performed (see Table C.1). As indicated in the table, three programs are considered: OpenSees (McKenna, 2011), DEEPSOIL (Hashash et al., 2020), and PySeismoSoil (Jsh9, 2023;

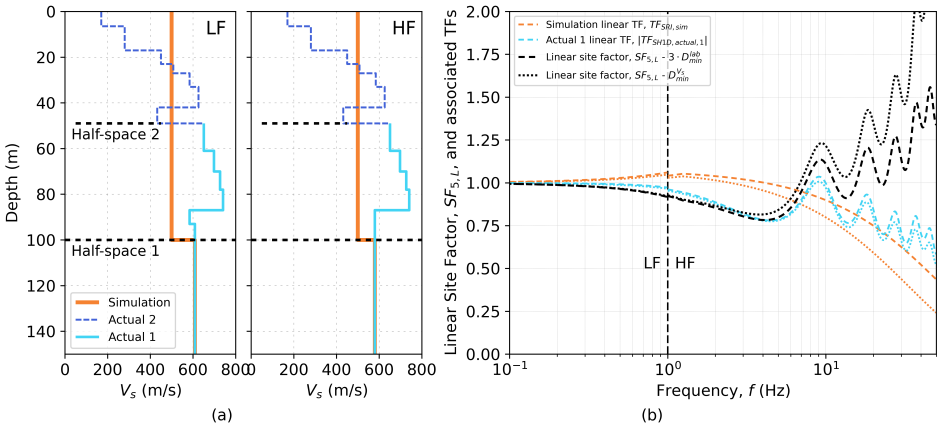

Figure C.37. (a) V_S profiles used in Methods 5 for the site RHSC, and (b) resulting linear site factor.

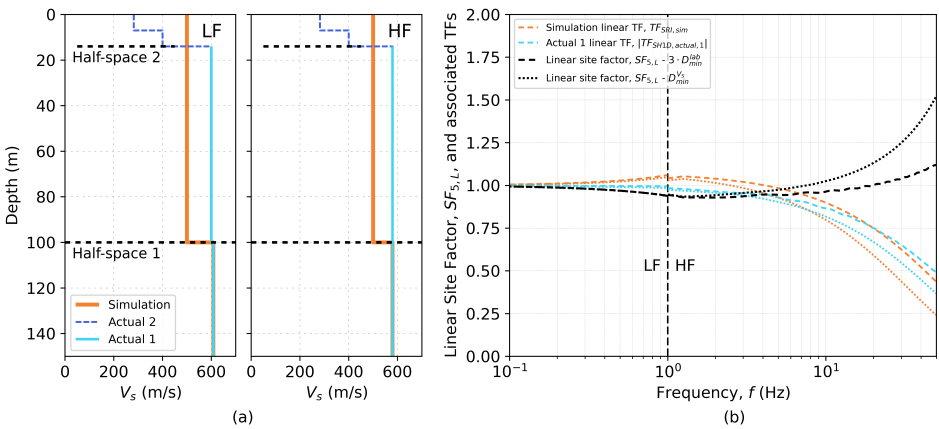

Figure C.38. (a) V_S profiles used in Methods 5 for the site CACS, and (b) resulting linear site factor.

Asimaki and Shi, 2017). OpenSees allows for the use of elastoplastic constitutive models, whereas DEEPSOIL and PySeismoSoil utilize cyclic stress-strain relationships, which are defined by a backbone curve and a series of rules that describe the hysteretic behavior of the soil. In OpenSees, the PressureDependMultiYield02 and PressureIndependMultiYield models (Yang et al., 2003, 2008) are used for granular and cohesive materials, respectively, and two different approaches to define the soil backbone curve are considered: (1) in Analysis 1, the octahedral shear strength of

the soil is prescribed through the input of friction angle or cohesion defined in octahedral space (Khosravifar, 2012; Khosravifar et al., 2018), which results in a code-generated hyperbolic backbone curve (Yang et al., 2003); (2) in Analysis 2, a user-defined modulus reduction (MR) curve is prescribed for each layer. Analysis 3 uses the General Quadratic/Hyperbolic (GQ/H) model (Groholski et al. 2016), implemented in DEEPSOIL, and Analysis 4 utilizes the Hybrid Hyperbolic (HH) model (Shi and Asimaki, 2017), implemented in PySeismoSoil.

Table C.1. Different software programs and constitutive models investigated for 1D time-domain nonlinear site-response analysis in Method 5.

Analysis	Program	Constitutive model	
1	OpenSees (McKenna 2011)	PressureDependMultiYield02 (PDMY02) Model for granular materials (Yang et al., 2008) PressureIndependMultiYield (PIMY) Model for cohesive materials (Yang et al., 2008)	Code-generated hyperbolic backbone curves
2			User-defined MR curves
3	DEEPSOIL (Hashash et al. 2020)	General Quadratic/Hyperbolic (GQ/H) model (Groholski et al. 2016)	
4	PySeismoSoil (Jsh9 2023; Asimaki and Shi 2017)	Hybrid Hyperbolic (HH) Model (Shi and Asimaki 2017)	

For Analyses 2 to 4, the backbone curve (or, equivalently, the MR curve) of each layer for the small-to-moderate strain range was defined based on the Darendeli (2001) model, and in the large strain range this relationship was adjusted for consistency with the shear strength of the soil, although using different procedures in each case (Yee et al. 2013; Groholski et al. 2016; Shi and Asimaki 2017, respectively). This ensures consistency between the backbone curves used in Analyses 2 to 4, particularly in the small- and large-strain ranges, although some considerable differences can be produced in the transition strain range, due to the use of different procedures. On the other hand, Analysis 1 is based on the hyperbolic model, and therefore, significant differences with the other analyses are expected.

Regarding the small-strain damping implementation, Rayleigh damping was adopted in OpenSees and DEEPSOIL, using an average value of the $D_{min,actual}$ profile, and selecting the target frequencies according to Kwok et al. (2007), whereas the Liu and Archuleta (2006) formulation was used in PySeismoSoil, which utilizes the entire $D_{min,actual}$ profile as input. For both the simulation and actual profiles, D_{min} was estimated using D_{min}^{lab} with a multiplicative factor of 3 (Pretell et al. 2023).

Figures C.39 to C.42 compare the resulting amplification factors for the four analyses and four sites considered. Figure C.39 shows that for PRPC the amplification factors obtained by Analyses 2 to 4 are very similar, and they depart significantly from Analysis 1 in some cases, illustrating how the variability between codes and models can be significantly reduced when consistent backbone curves are considered.

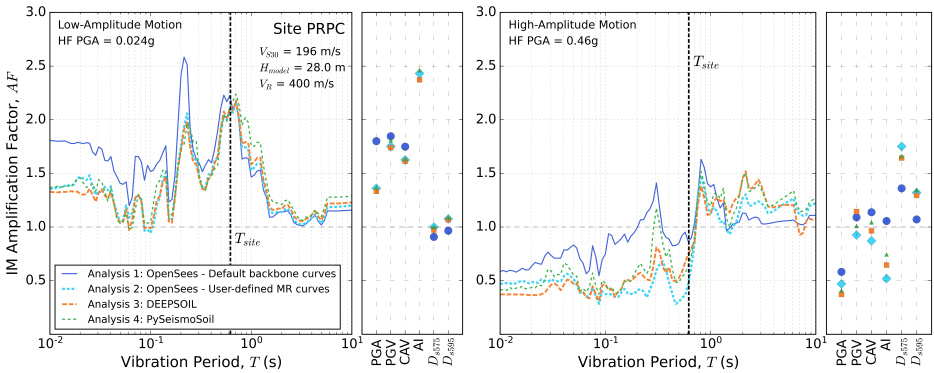

Figure C.39. Amplification factors of different IMs resulting from applying Method 5 to the sites PRPC, for different site-response analysis codes and constitutive models.

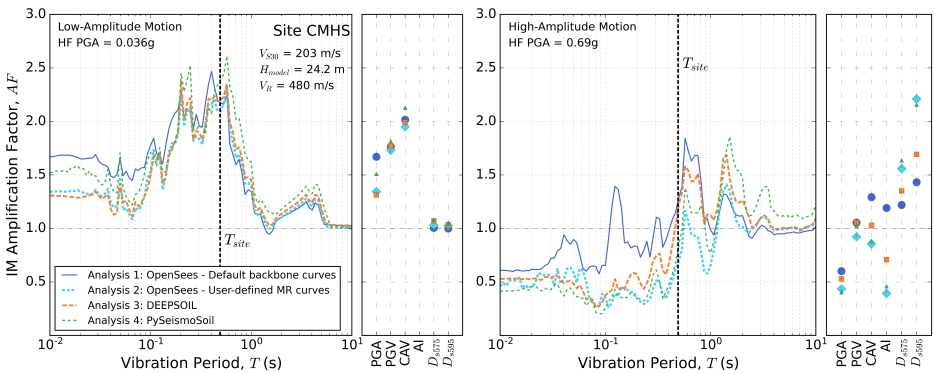

Figure C.40. Amplification factors of different IMs resulting from applying Method 5 to the sites CMHS, for different site-response analysis codes and constitutive models.

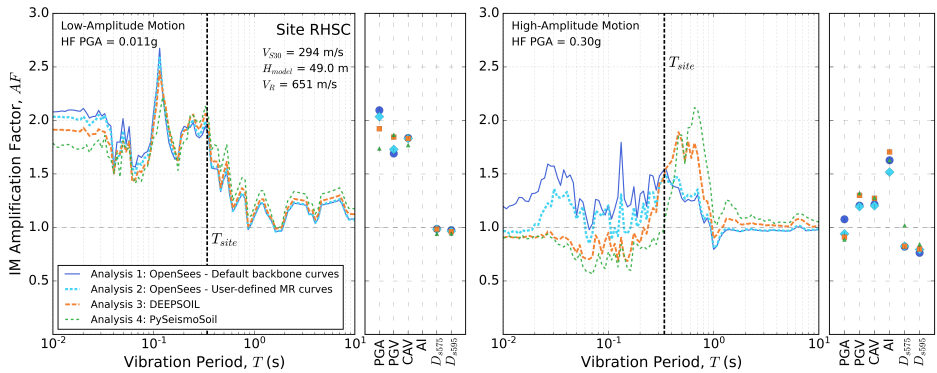

Figure C.41. Amplification factors of different IMs resulting from applying Method 5 to the sites RHSC, for different site-response analysis codes and constitutive models.

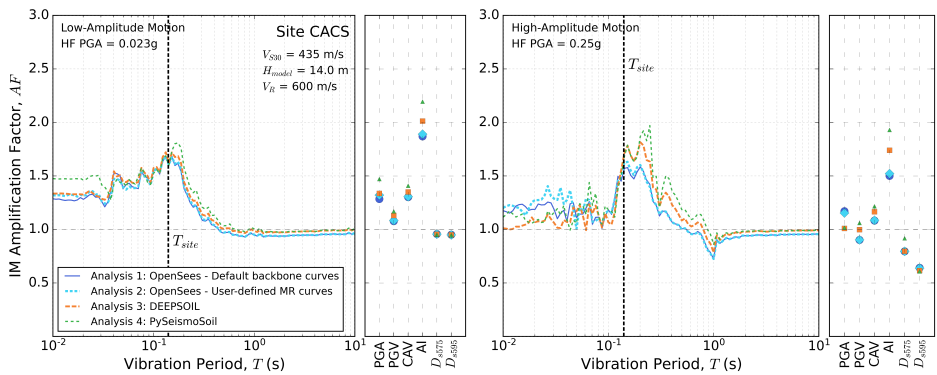

Figure C.42. Amplification factors of different IMs resulting from applying Method 5 to the sites CACS, for different site-response analysis codes and constitutive models.

C.7 Comparison between methods

Figure C.43 and C.44 superimpose the SA amplification factors (AFs) and the site factors (SFs), for the low- and high-amplitude motion, respectively, for Methods 1 to 4. In the case of the AFs the x-axis represents the oscillator vibration periods, whereas for the SFs this axis represents the periods of the ground motion in the Fourier domain. These figures illustrates how the SF at a given period impact the AF at the equivalent oscillator period.

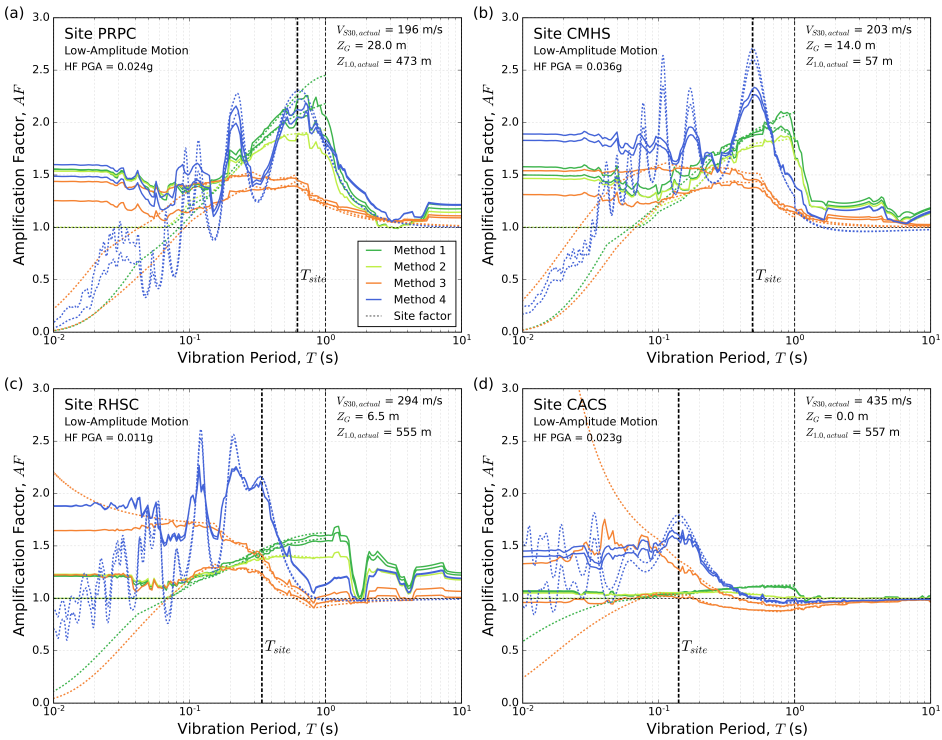

Figure C.43. Comparison between the SA amplification factors (continuous lines) and the site factors (dashed lines) for Methods 1 to 4, for the low-amplitude motion. Results for the sites (a) PRPC, (b) CMHS, (c) RHSC, and (d) CACS. Site factors of Methods 1 and 2 are plotted up to a vibration period of 1 s to illustrate that their applications was limited to the HF range.

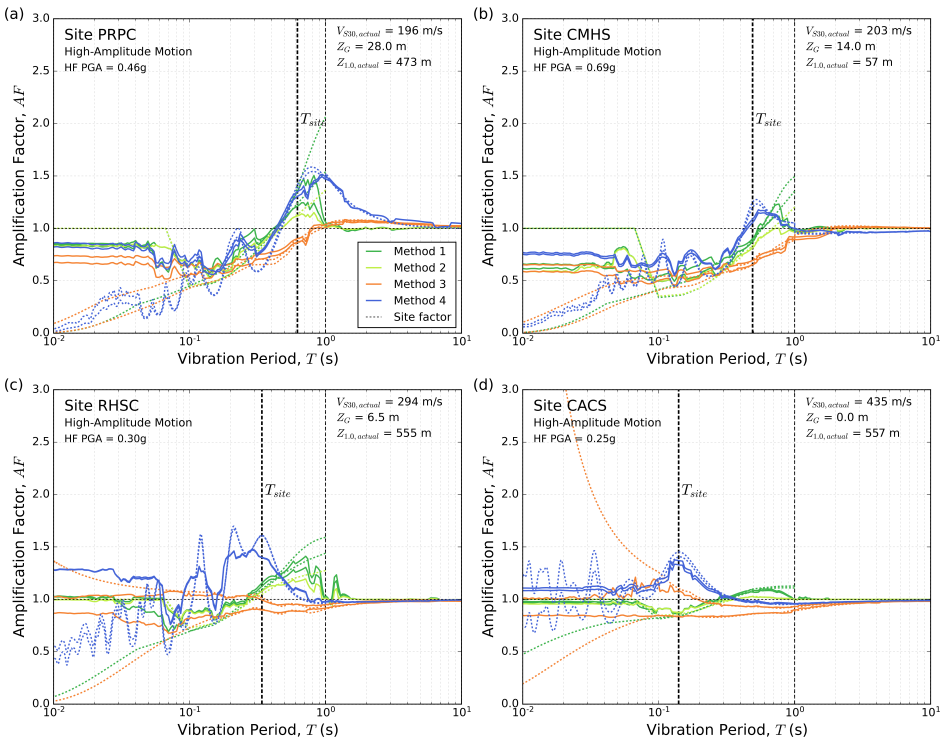

Figure C.44. Comparison between the SA amplification factors (continuous lines) and the site factors (dashed lines) for Methods 1 to 4, for the high-amplitude motion. Results for the sites (a) PRPC, (b) CMHS, (c) RHSC, and (d) CACS. Site factors of Methods 1 and 2 are plotted up to a vibration period of 1 s to illustrate that their applications was limited to the HF range.

C.8 Additional References in the Electronic Supplements

The following are the additional references cited in the Electronic Supplements, which complement the main references of the paper.

Asimaki D and Shi J (2017) SeismoSoil User Manual, v1.3.

Khosravifar A (2012) Analysis and design for inelastic structural response of extended pile shaft foundations in laterally spreading ground during earthquakes. PhD Thesis. University of California, Davis.

Khosravifar A, Elgamal A, Lu J and Li J (2018) A 3D model for earthquake-induced liquefaction triggering and post-liquefaction response. Soil Dynamics and Earthquake Engineering 110:43–52.

Kwok AOL, Stewart JP, Hashash YMA, Matasovic N, Pyke R, Wang Z and Yang Z (2007) Use of Exact Solutions of Wave Propagation Problems to Guide Implementation of Nonlinear Seismic Ground Response Analysis Procedures. Journal of Geotechnical and Geoenvironmental Engineering 133(11): 1385–1398.

Liu P and Archuleta RJ (2006) Efficient Modeling of Q for 3D Numerical Simulation of Wave Propagation. Bulletin of the Seismological Society of America 96(4A): 1352–1358.

McGann CR, Bradley BA, Taylor ML, Wotherspoon LM and Cubrinovski M (2015) Development of an empirical correlation for predicting shear wave velocity of Christchurch soils from cone penetration test data. Soil Dynamics and Earthquake Engineering 75: 66–75.

Robertson PK (2009) Interpretation of cone penetration tests — a unified approach. Canadian Geotechnical Journal 46(11): 1337–1355.

Van Ballegooy S, Cox SC, Thurlow C, Rutter HK, Reynolds T, Harrington G, Fraser J and Smith T (2014) Median water table elevation in Christchurch and surrounding area after the 4 September 2010 Darfield Earthquake. Version 2 edition. Lower Hutt, New Zealand: GNS Science. ISBN 978-1-927278-41-3. OCLC: 889582289.

Westerhoff R, White P and Miguez-Macho G (2018) Application of an improved global-scale groundwater model for water table estimation across New Zealand. Hydrology and Earth System Sciences 22(12): 6449–6472.